

Article

Evaluating the Applicability of Global LULC Products and an Author-Generated Phenology-Based Map for Regional Analysis: A Case Study in Ecuador's Ecoregions

Gladys Maria Villegas Rugel ^{1,2,*}, Daniel Ochoa ², Jose Miguel Menendez ^{2,3} and Frieke Van Coillie ¹

¹ Remote Sensing, Spatial Analysis Lab (REMOSA), Department of Environment, Ghent University, 9000 Ghent, Belgium; frieke.vancoillie@ugent.be

² Facultad de Ingeniería en Electricidad y Computación, Campus Gustavo Galindo, ESPOL Polytechnic University, Km. 30.5 Vía Perimetral, Guayaquil 090101, Ecuador; dochoa@fiee.espol.edu.ec (D.O.); josemiguel.menendezsanchez@ugent.be (J.M.M.)

³ Department of Telecommunications and Information Processing, Interuniversity Microelectronics Centre, Ghent University/IMEC, 9000 Ghent, Belgium

* Correspondence: gladysmaria.villegasrugel@ugent.be

Abstract: An accurate and detailed understanding of land-use change affected by anthropogenic actions is key to environmental policy decision-making and implementation. Although global land cover products have been widely used to monitor and analyse land use/land cover (LULC) change, the feasibility of using these products at the regional level needs to be assessed due to the limitation and biases of generalised models from around the world. The main objective of the present study was to generate regional LULC maps of three target areas located in the main ecoregions of Ecuador at a resolution of 10 m using Google Earth Engine (GEE) cloud-based computing. Our approach is based on (1) Single Date Classification (SDC) that processes Sentinel-2 data into fuzzy rule-driven thematic classes, (2) rule refinement using Visible Infrared Imaging Radiometer Suite (VIIRS) data, and (3) phenology-based synthesis (PBS) classification that combines SDC into LULC based on the occurrence rule. Our results show that the three target areas were classified with an overall accuracy of over 80%. In addition, cross-comparison between the global land cover products and our LULC product was performed and we found discrepancies and inaccuracies in the global products due to the characteristics of the target areas that included a dynamic landscape. Our LULC product supplements existing official statistics and showcases the effectiveness of phenology-based mapping in managing land use by providing precise and timely data to support agricultural policies and ensure food security.

Keywords: LULC; phenology-based algorithm; image classification; GEE; Sentinel-2



Citation: Villegas Rugel, G.M.; Ochoa, D.; Menendez, J.M.; Van Coillie, F. Evaluating the Applicability of Global LULC Products and an Author-Generated Phenology-Based Map for Regional Analysis: A Case Study in Ecuador's Ecoregions. *Land* **2023**, *12*, 1112. <https://doi.org/10.3390/land12051112>

Academic Editor: Chandra Giri

Received: 12 April 2023

Revised: 11 May 2023

Accepted: 16 May 2023

Published: 22 May 2023



Copyright: © 2023 by the authors. Licensee MDPI, Basel, Switzerland. This article is an open access article distributed under the terms and conditions of the Creative Commons Attribution (CC BY) license (<https://creativecommons.org/licenses/by/4.0/>).

1. Introduction

Land cover provides important biophysical properties to the Earth's surface [1]. Land cover changes, either natural or human-made, may have negative socioeconomic and environmental impacts [2] at global and regional levels. In the latter case, local decision-makers need accurate and timely land change information to design management policies and plans for a range of issues such as sustainable use of natural resources, agricultural production, and emergency response, among others. In practice, spatial information on physical land covers is compiled in Land Use and Land Cover (LULC) maps which are built upon satellite images captured over a given period of time.

The availability of various types of satellite data has prompted a number of global land cover (GLC) mapping initiatives at different spatial and temporal resolutions. Coarse spatial resolution initiatives include the global land cover classification 2000 (GLC2000) [3] and the International Geosphere-Biosphere Programme DISCover land cover classification

(IGBPDISCover) [4], both at 1 km resolution. Moderate Resolution Imaging includes the Imaging Spectroradiometer land cover (MOD12Q1) [5] at 500 m resolution, and the global land cover map (GlobCover) [6] at 300 m resolution. More recently, higher resolution (20–30 m) GLC maps based on Landsat and Sentinel data have become available. The Esri 2020 landcover (Esri-GLC) [7], ESA WorldCover 2020 (WC) [8], and Dynamic World (DW) [9] report 10 m, the finest granularity accomplished to date in GLC mapping. Despite their increasing spatial resolution, global LULC products at the regional level show inaccuracies. Previous studies have highlighted significant differences in land class mapping between different global products. For example, a study conducted in Syria found large discrepancies in land class mapping between Esri-GLC and WC global products [10]. Additionally, another study reported low accuracy for three high-resolution GLC products in the southwest China region [11]. These findings underscore the need for more accurate and consistent GLC mapping efforts.

Besides spatial resolution, the LULC map quality depends on the pixel classification technique [12]. When enough training samples are available, supervised learning methods have been proposed for classification. Otherwise, unsupervised classifiers are used, which do not require training samples. Various supervised and unsupervised classification techniques have been evaluated on several satellite images for LULC mapping tasks in previous studies [13–18]. Recently, phenology-based classification approaches have shown high discriminative power [19,20]. They exploit metrics that describe critical moments of the phenological cycles over time to detect land changes in image time series. Among them, the start, peak, end, and duration of a season, as well as statistics of spectral indices, have been proposed to detect various LULC types. Previous work has produced LULC maps at regional and local scales with a high spatial resolution by using commercial satellite data [17,21–23] or by adding alternative data sources [24–28]. Replicating these approaches is a challenging task for many public institutions in developing countries. One such challenge is the difficulty in accessing clear satellite images, particularly during the rainy/wet season, which is a common issue faced by many developing countries in Sub-Saharan Africa [29]. Furthermore, in South America, only a few region-level products have been developed [30]. The latest, yet global, LULC map that includes Ecuador was created in 2014 using RapidEye and Landsat-8 satellite imagery.

This study explores the challenges of phenology-based classification to obtain a reliable classification at the regional level in Ecuador that reflects well-known seasonal variations. Our approach consists of three steps: (1) single data classification of Sentinel-2 data into thematic classes driven by fuzzy rules using monthly images; (2) rule refinement using VIIRS data; (3) phenology-based synthesis into LULC based on recurrence rules. We compare our results against three 10 m global products: WC, DW, and Esri-GLC. By using phenological information extracted from high-resolution satellite imagery, we were able to describe land use at a generic level. LULC mapping results support a paradigm shift from standard static products to the generation of large-scale dynamic on-demand LULC maps through advanced cloud computing resources that have become readily available as cloud services.

2. Materials and Methods

2.1. Target Areas

In each of the three main ecoregions of Ecuador—the coast, the Andean highland, and the Amazon ecoregion—one study area was allocated. On the coast, a 463.03 km² area is located in the Daule district. The Ecuadorian coast has two seasons: the rainy season with tropical heat and high humidity that goes from December to April, and the dry slightly cooler season that extends from May to December. The annual average precipitation level is 1007 mm and temperatures range from 20 °C to 27 °C most of the year [31]. Based on previous studies [32], it was found that approximately 80% of Daule’s land consists of agricultural areas, primarily rice crops, along with some areas dedicated to maize and fruit tree cultivation.

Near Cayambe city in the northern Ecuadorian Andes, an area of 447.17 km², including the 5790 m high Cayambe volcano was used in our experiments. In the Andean highland, the rainy season runs from September to April. Annual rainfall levels range from 250 to 2000 mm. The dry period, from June to August, is characterised by strong winds and high-intensity solar radiation. Across inter-Andean valleys, the temperature goes from 12 °C to 18 °C, but at higher altitudes, the temperature drops to 5 °C [31]. In the Andean highlands, vegetation mostly consists of grasslands, shrublands, wetlands, and small areas of high Andean forests [33].

The last study area (150.85 km²) is located in Joya de los Sachas, a sparsely populated district in the Ecuadorian Amazon basin. Tropical rainforest climate produces annual rainfall levels from 2500 to 4000 mm during the rainy season from May to December. However, non-seasonal rainfalls are very common [34]. Fog and clouds usually cover the higher lands, whereas average annual precipitation and temperature levels correspond to 2942 mm and 29.7 °C, respectively, [31]. Joya de los Sachas's land is mostly covered by tropical forests and plots of small-scale crops such as African palm, cocoa, and maize [35]. In this paper, each target area is referred to by its ecoregion: the coast, the Andean highland, and the Amazon. Figure 1 shows their location and a sample satellite image.

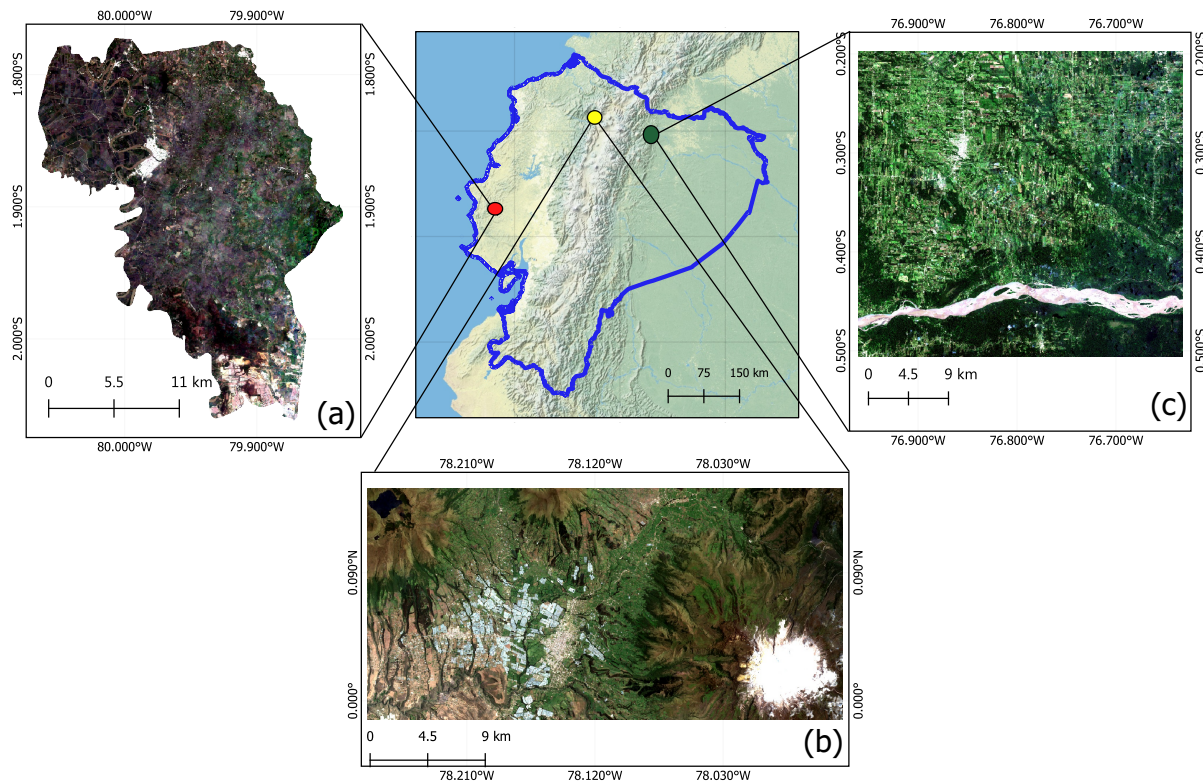


Figure 1. Location of the target areas in Ecuador, representing three distinct ecoregions: (a) Daule, located in the Pacific coast; (b) Cayambe, situated in the Andean highland; (c) Joya de los Sachas, located in the Amazon rainforest ecoregion.

2.2. Datasets

To capture the spectral signatures of vegetation and soil caused by seasonal variations, we use 2019 and 2020 Sentinel-2 and VIIRS imagery collections. In previous works [36–38], the information contained in these datasets has improved spatial coherence and detailed characterisation of land. Moreover, they are freely available from the GEE satellite imagery catalogue and can be readily accessed using GEE's application programming interface.

Sentinel-2 collection: It has 10–60 m spatial, five-day temporal, and 13-band spectral resolutions. In humid tropical regions, optical data show chronic cloud cover [39]. Persistent clouds and shadows distort multitemporal image mosaics, reducing the accuracy of LULC

mapping types. Figure 2 shows the percentage of the monthly average cloud cover in the target areas during the studied period. As expected, Amazon's target area shows the highest cloud contamination, reaching up to 98% cloud cover between January and June.

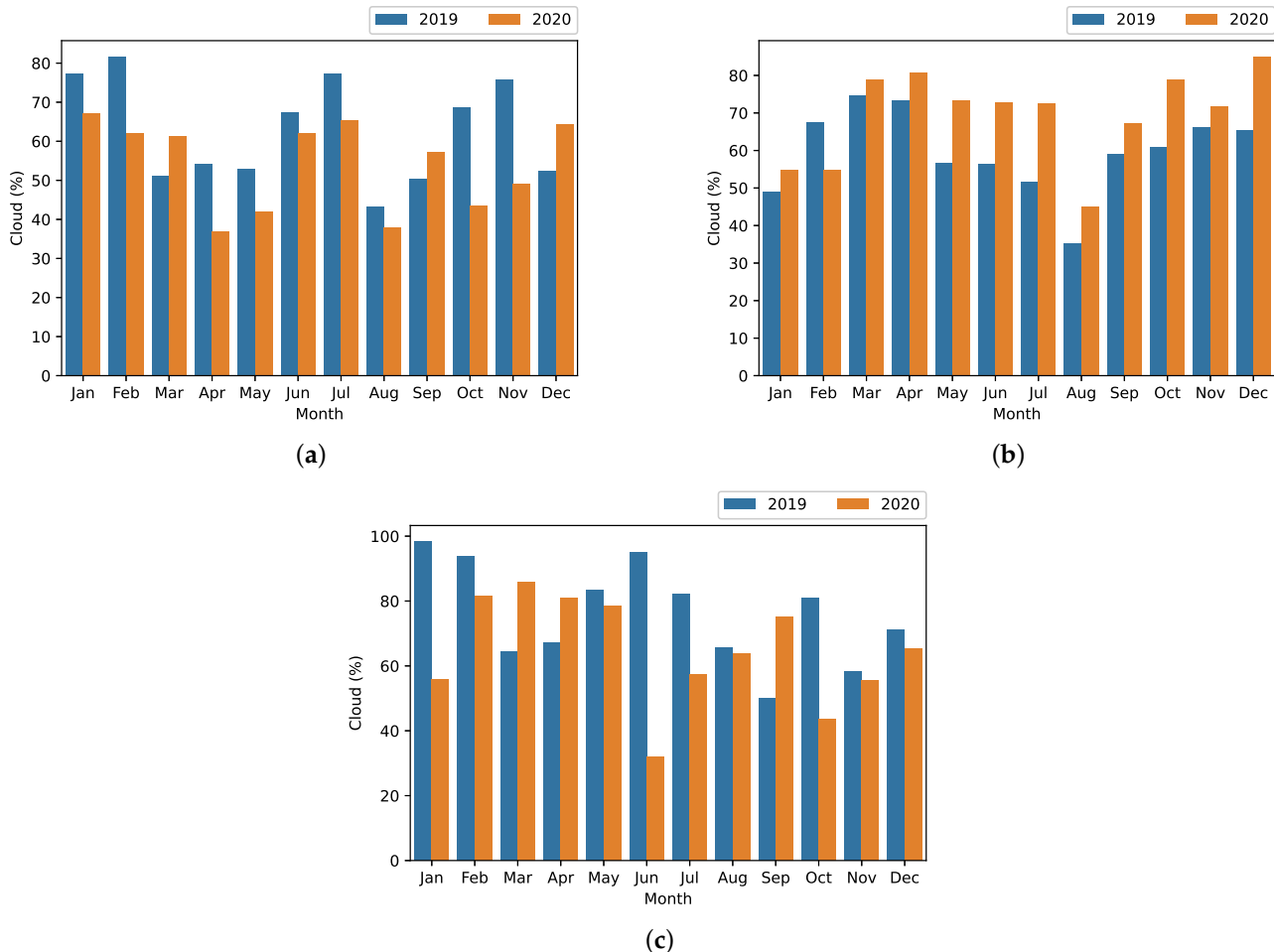


Figure 2. Sentinel-2 image cloud over the target areas in (a) coast, (b) Andean highland, and (c) Amazon.

VIIRS Day/Night Band (DNB) collection: Sourced from the Suomi National Polar-orbiting Partnership (Suomi-NPP) satellite, it provides multitemporal night time light (NTL), for near real-time monitoring of nocturnal visible and near-infrared light [40]. We use the VIIRS DNB Monthly Composites Version 1 data produced in geographic grids of 15 s of arc (approximately 500 m at the Equator), covering the globe from 75 N to 65 S latitudes. They contain two bands, the mean DNB radiance values and the amount of cloud-free cover.

2.3. Classification Scheme and Reference Data

Our classification scheme is based on [41], which generates a land cover map in two steps by applying SDC and PBS algorithms sequentially. To effectively support resource planning tasks, we extend these algorithms by adding the land use classes. For SDC, we added the agriculture, greenhouse, and urban area classes and for the PBS annual crops, perennial crops and urban areas were added. Table 1 lists the LULC classes to be detected. The second column indicates the LULC classes output by our extended SDC algorithm and the third column lists the final LULC classes obtained after PBS classification. The latter classes should enable the resulting LULC maps to be used as input data for advanced

applications; for instance, land differentiation of annual crops, detection of agricultural mode, and measuring the impact on biogeochemical cycles.

Table 1. Thematic classes used in the SDC and PSB classifier.

Class	Algorithm		Type
	SDC	LULC-PBS	
Clouds	x		-
Water	x	x	Land cover
Snow	x	x	Land cover
Dark vegetation	x		Land cover
Low IL	x		Land cover
Dark soil	x		Land cover
Bright soil	x		Land cover
Grass	x		Land cover
Bright forest	x		Land cover
Pure forest	x		Land cover
Sparse	x		Land cover
Shadow soil	x		Land cover
Degraded forest	x		Land cover
Shrub	x	x	Land cover
Forest		x	Land cover
Agriculture *	x		Land use
Built-up *	x		Land use
Greenhouse *	x	x	Land use
Annual Crop *		x	Land use
Perennial Crop *		x	Land use
Grassland		x	Land cover
Bare soil		x	Land cover
Urban areas *		x	Land use

* Classes created in this study.

To characterise LULC classes, reference points were sampled evenly across the target areas. For each target area, a set of ground truth reference points was built based on the author's knowledge and visual interpretation of high-resolution composite images created with Google Earth Pro (version 7.3.2.5776) [42,43]. These composite images were generated from 2019 and 2020 imagery of satellite and aircraft data at resolutions between 15 cm and 30 m with the built-in timeline tool of the Google Earth Composite Editor.

For the SDC algorithm, 1500 pixels were used to evaluate spectral indices used in land cover classification rules. These pixels were labelled as soil, water, built-up, agriculture, and greenhouse and were distributed in 300, 300, 300, 500, and 100 pixels, respectively. Within the agriculture pixel group, banana and cocoa crop pixels were selected to represent perennial crops; rice and maize crop pixels were selected to represent annual crops. Samples of perennial crops were not included in the target area of the Andean highlands, as only greenhouses occur in the target area. The remaining 14 thematic classes were characterised in Simonetti et al. [41]. As for the PBS algorithm, we used 100 pixels for each LULC-PBS class in the different areas to build the classification rules. Besides, we selected 2400 independent reference pixels for the validation of our LULC-PBS maps, i.e., 100 pixels corresponding to each class and target area. Perennial crop sample points were collected only on the coast and Amazon. Snow reference points were extracted only in the Andean highland.

2.4. Methodology

The methodology of this study is depicted in Figure 3. As a preprocessing step, Sentinel-2 images were filtered to reduce the influence of clouds. The set of monthly composite images was built as follows. First, Sentinel 2 images with higher cloud cover from 50% to 70%, depending on the region, were discarded. For the remaining images, see

Table 2, cloudy pixels were masked using the QA60 bitmask band (a quality flag band) that is provided as metadata in Sentinel 2 products. Then, same-month images were merged using the median function of the GEE image reducer software. Finally, spectral indices listed in Table 3 were computed. Regarding VIIRS images, they were resampled to 10 m using bilinear interpolation to match the spatial resolution of Sentinel-2.

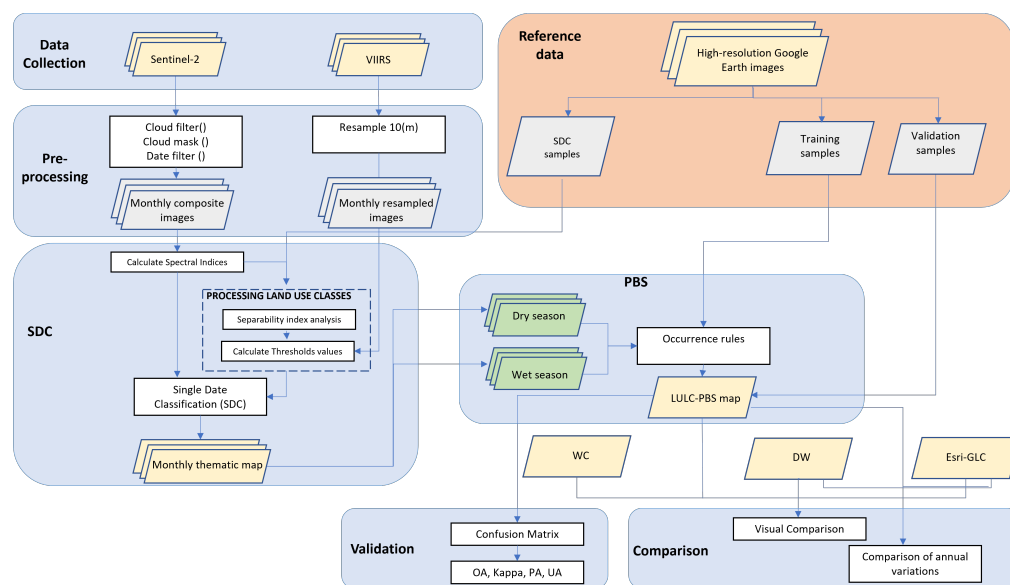


Figure 3. Overview of the proposed methodology for LULC mapping.

Table 2. Sentinel-2 dataset before and after pre-processing, including the number of images in the dataset for each target area.

Area	2019		2020	
	Original	Final	Original	Final
Coast	504	113	512	133
Andean highland	296	40	284	38
Amazon	153	27	159	43
Total	953	180	955	214

LULC class discrimination was evaluated using separability index analysis on spectral indices. From this analysis, suitable threshold values for the SDC algorithm were estimated (Section 2.4.1). For each target area, the resulting thematic maps were grouped into dry and wet season sets to capture phenological characteristics that were later exploited for PBS classification (Section 2.4.2). On the resulting LULC product, which we refer to in the rest of the document as the LULC-PBS map, we performed statistical validation using well-known detection accuracy metrics (Section 2.4.3). Finally, a comparison against global LULC products at 10 m spatial resolution was conducted (Section 2.4.4).

2.4.1. SDC

We applied SDC to detect LULC classes using the rule-based approach proposed by Simonetti et al. [44] in the construction of the SDC algorithm. Classification rules compare a pixel’s spectral indices against a set of given empirical threshold values that were set using global scale observations. To Simonetti’s 14 SDC land cover classes, listed in Table 1, we added built-up, agriculture, and greenhouse classes to better represent the actual land use types in Ecuador. For these new classes, we chose spectral indices and thresholds by quantifying interclass separability from the spectral indices listed in Table 3. It should be emphasised that our extended set of SDC classes is not present in the final LULC-PBS map, but they are rather used to build the recurrence rules that guide its construction.

Spectral index selection was performed using the Bhattacharyya distance, usually referred to as *Score*. It measures the scatter degree between two classes (ω_i, ω_j), as follows:

$$Score(\omega_i, \omega_j) = -\log \int \sqrt{(p(x|\omega_i)p(x|\omega_j))} dx. \quad (1)$$

where, $p(x|\omega_i)$ and $p(x|\omega_j)$ are the prior conditional probability of the classes ω_i and ω_j , respectively, with $i \neq j$. In contrast to other methods for measuring class separability, such as divergence, transformed divergence, and the Jeffries–Matusita distance [45–49], the Bhattacharyya covers the interval $[0, \infty]$, i.e., it has no upper limit, therefore allowing it to identify the highest spectral separability between indices. The higher the score the easier to discriminate between two classes.

Table 3. Spectral indices used in this study: SWIR1, SWIR2, NIR, RED, GREEN, and BLUE represent the spectral reflectance in the shortwave infrared 1, shortwave infrared 2, near-infrared, red, green, and blue bands, respectively. These correspond to the B11, B12, B8, B4, B3, and B2 spectral bands of the Sentinel-2 MSI sensor.

Index	Equation	Ref.
Normalised difference vegetation index (NDVI)	$\frac{(NIR-RED)}{(NIR+RED)}$	[50]
Bare soil index (BSI)	$\frac{(RED+SWIR1)-(NIR+BLU)}{(RED+SWIR1)+(NIR+BLU)}$	[51]
Urban index (UI)	$\frac{(SWIR2-NIR)}{(SWIR2+NIR)}$	[52]
Normalised difference built-up index (NDBI)	$\frac{(SWIR1-NIR)}{(SWIR1+NIR)}$	[53]
Normalised difference tillage index (NDTI)	$\frac{(SWIR1-SWIR2)}{(SWIR1+SWIR2)}$	[54]
Normalised difference water index (NDWI)	$\frac{(GREEN-NIR)}{(GREEN+NIR)}$	[55]
Normalised difference snow index (NDSI)	$\frac{(GREEN-SWIR)}{(GREEN+SWIR)}$	[56]
Green difference vegetation index (GDVI)	$\frac{(NIR-GREEN)}{(NIR+GREEN)}$	[57]
Soil-adjusted vegetation index (SAVI)	$\frac{(NIR-RED)(1+L)}{(NIR+RED+L)}$	[58]
Enhanced vegetation index (EVI)	$\frac{2.5(NIR-RED)}{NIR+(C1 \times RED)-(C2 \times BLUE)+L}$	[59]

In our separability analysis for built-up pixels, we include water, dark soil, and bright soil because it is well-known that pixels along river banks tend to show similar spectral indices values. After the most discriminant spectral indices for each SDC class were found on the monthly image stack, rules were drawn by comparing spectral indices boxplots. Due to the characteristics of Ecuador’s target areas, threshold values must be set according to phenological cycles and geographic, climatic, and seasonal conditions.

2.4.2. PBS

LULC classification using phenology-based synthesis is performed by extracting and testing for recurrence patterns in SDC labels over time. The SDC provides land cover classification based on a single image, whereas PBS leverages temporal patterns to improve classification accuracy. Such patterns can be formulated as rules that are pixel-wise evaluated across an SDC thematic map stack. If all conditionals in a rule are true at a given location, the corresponding LULC-PBS class is assigned to that pixel in the LULC-PBS map. Table 1 shows the LULC-PBS classes defined for this study. To build a recurrence rule (see

Figure 4), we used empirical thresholds based on observations from SDC monthly thematic maps grouped into dry and wet seasons and collected at the regional scale.

Few rules are independent of the target area under study. For instance, water is a very stable class, as pixels classified as water appear at the same locations across every stack and target area. Forest, grassland, shrub, bare soil, and urban rules combine a number of SDC classes but show similar frequency patterns in all target areas. Annual crops use different recurrence rules per target area because seasonal and geographical conditions influence spectral index values and consequently SDC output as seen in Figure A1, Appendix A. For instance, on the coast, annual crops occur when at least 10% of degraded forest and 50% of agriculture labels appear per pixel location, followed by observations of up to 50% of water, 40% grass, 30% bright soil, 20% bright forest, and up to 10% dark vegetation as sparse, as shown in Figure 4a. If the same pixel is labelled as cloud at least 80% of the time across a stack, that pixel is marked as No Data. Our PBS classification routine was coded using the GEE framework with JavaScript language.

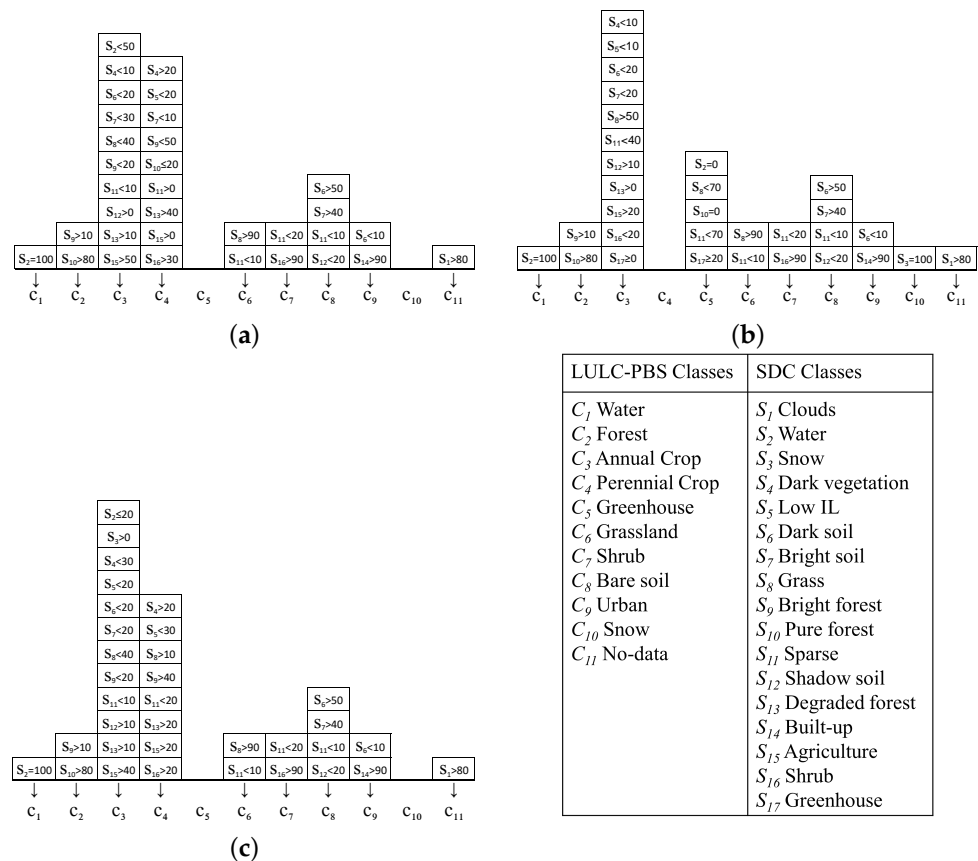


Figure 4. Recurrence rules for LULC-PBS classes, with the percentage of observations per SDC thematic class (legend indicates classes used in SDC and PSB classifier) in (a) coast, (b) Andean highland, and (c) Amazon. Percentages are used to express values.

2.4.3. Accuracy Metrics

LULC-PBS map accuracy was evaluated using four confusion metrics: overall accuracy (OA), producer accuracy (PA), user accuracy (UA), Kappa coefficient, and F1-score. OA is the probability that a pixel, taken at random from the classified data, has the same class as the corresponding pixel in the reference data and vice versa. PA is the probability that a pixel from the reference data class i belongs to the same class in the classified data. It indicates how well the reference data of a class are classified. UA is the probability that a pixel from the classified data class i belongs to the same class in the reference data. It indicates the probability that a classified pixel actually represents class i on the ground truth data. Kappa indicates the proportional reduction in the error generated by a classification,

compared to the error of a completely random classification [60]. F1-score is the harmonic mean of precision and recall, which are measures of the accuracy and completeness of the classification, respectively. This score varies between 0 (lowest value) and 1 (best value).

2.4.4. LULC Maps Comparison

To evaluate the spatial coherence of LULC products at each target area, we split them into three sub-areas that displayed all LULC-PBS classes as follows (Table 4):

Table 4. Mathematical models for each target area and their corresponding sub-areas. The sub-areas used in this modelling process can be visualised in Figure 8.

Target Area	Sub-Areas
Coast	$A^C = \{A_1^C, A_2^C, A_3^C\}$
Andean Highland	$A^H = \{A_1^H, A_2^H, A_3^H\}$
Amazon	$A^A = \{A_1^A, A_2^A, A_3^A\}$

First, we visually compared LULC-PBS, Esri-GLC (global), DW, and WC maps for 2020 against Google Earth imagery. Although somewhat limited, this type of analysis provides insights into the spatial matching of LULC labels. In a more quantitative evaluation, the spatiotemporal variation in LULC classes was measured using the normalised variation index as follows. Given:

$r \in \mathcal{R} = \{C, H, A\}$, the name of a region: Coast C , Highlands H , or Amazon A .

$c \in \mathcal{C}_h$, a class in the set of the harmonised LULC classes, see Table 5.

$m \in \mathcal{M} = \{\text{LULC-PBS, Esri-GLC, DW}\}$ a given LULC map used for comparison.

$y \in \mathcal{Y} = \{2018, \dots, 2020\}$ a year in the evaluation period.

Table 5. Harmonised LULC classes of LULC-PBS, Esri-GLC, and DW.

\mathcal{C}_h	Harmonised Class	LULC-PBS	Esri-GLC	DW
c_{h_1}	Water	Water	Water	Water
c_{h_2}	Forest	Forest	Trees	Trees
c_{h_3}	Cropland	Annual crop	Flooded vegetation	Crops
		Perennial crop	Crops	Flooded vegetation
		Greenhouse		
c_{h_4}	Rangeland	Grassland	Rangeland	Grass
		Shrub		Shrub and Scrub
c_{h_5}	Bare soil	Bare soil	Bare ground	Bare ground
c_{h_6}	Urban	Urban	Built area	Built area
c_{h_7}	Snow/Ice	Snow/ice	Snow and ice	Snow and ice
c_{h_8}	Clouds	Clouds	Clouds	Clouds

Then, the j th sub-area A_j^r at region r , is the sum of surface patches a labelled with every possible harmonised class c , for a given map m and year y :

$$A_j^r = \sum_c m a_{c,j}^{r,y} \tag{2}$$

The difference in size of a harmonised class surfaces with respect to $y_o = 2017$ for sub-area A_j^r is:

$$\Delta_{m a_{c,j}^{r,y}} = \left| m a_{c,j}^{r,y} - m a_{c,j}^{r,y_o} \right|. \tag{3}$$

Hence, the normalised variation index with respect to the size of that sub-area is:

$$m\tilde{a}_{c,j}^{r,y} = \frac{\Delta_{m\tilde{a}_{c,j}^{r,y}}}{A_j^r}. \quad (4)$$

In our experiments, WC products were excluded due to a lack of annual datasets. Furthermore, instead of the global Esri-GLC map we used the annual Esri-GLC product (2017–2021) which uses an updated 9-class model and combines Grass and Scrub into a single Rangeland class. The original Esri 2020 Land Cover collection uses a 10-class model (Grass and Scrub separately).

3. Results

3.1. Rules for New SDC Classes

To build SDC rules included in Algorithm 1 for agriculture, built-up, and greenhouse classes, first, we sought suitable indices for classification, and then we tried, across monthly images, combinations of rules and thresholds that deliver the best detection results. For instance, the built-up classification rule for the coast was developed using UI, NDBI, and BSI indices, as water and built-up pixels are largely separable with UI and NDBI indices, whereas soil and water pixels can be discriminated with the BSI index; see Figure 5a. First, we split the monthly image stack into dry and wet seasons to account for changes in solar radiation. Then, we found the index's value ranges that detect built-up pixels while filtering out the others; see Figure 6a. These ranges are added to the rule using AND operators. Finally, season rules are merged together using OR operators. If the final output requires additional refinement, we can add additional factors to the rule using the remaining indices and data sources. In the built-up class, we included VIIRS Nighttime Day/Night composite dataset values.

We repeated the aforementioned procedure for agriculture and greenhouse classes. In Ecuador, the agriculture class includes cocoa, banana, maize, and rice crops. For each target area, we compute the following vegetation indices: EVI, SAVI, GDVI, and NDVI. Some crops are easily distinguished from others such as rice in the coast and Amazon regions; see Figure 5b. However, in general, the ranges of spectral indices coincide across target areas which yields more compact rules than built-up class; see Figure 6b. Finally, the greenhouse class was computed with the same vegetation indices as agriculture class and only in the Andean highland ecoregion. The list of SDC rules is shown in Algorithm 1.

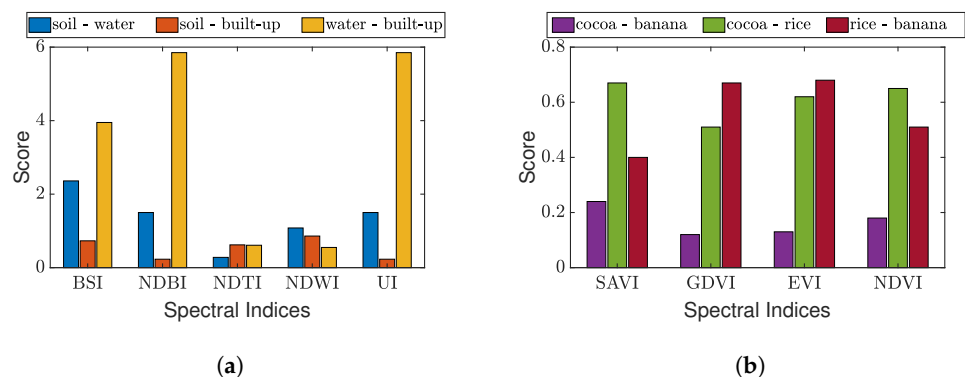


Figure 5. Bhattacharyya scores for (a) new land cover and (b) crop pixels in the coast target area.

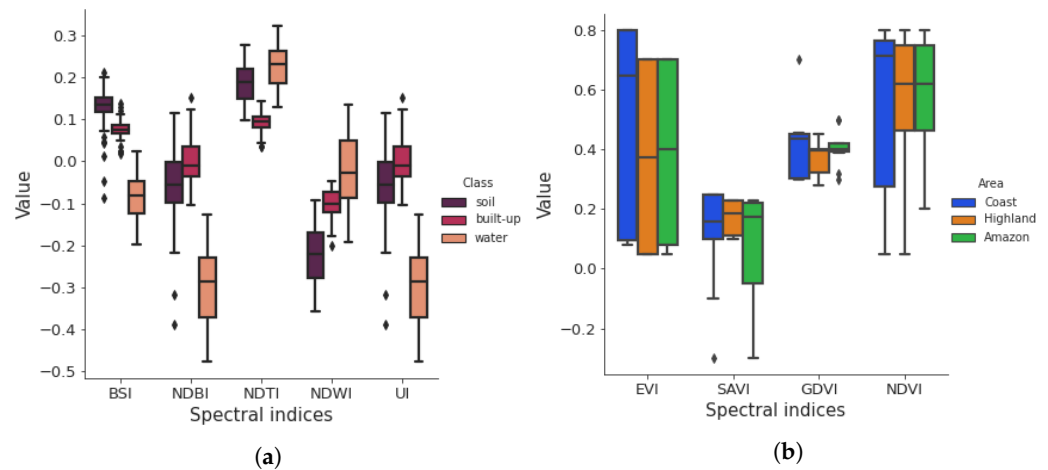


Figure 6. Spectral index boxplots: (a) land cover pixels and (b) for agriculture pixels in each target area.

Algorithm 1: SDC rules.

```

Input: UI, BSI, NDBI, NDVI, NDWI, EVI, SAVI, GDVI, EVI, NDTI, VIIRS
Output: OutClass
Data: Target area dataset
1 if Area is 'Coast' then
2   if ((UI>-0.05) and (NDBI >-0.13)) or ((BSI>-0.1 and BSI<0.1) and (VIIRS>20) and
   (NDTI <0.19)) then
3     OutClass = Built-up
4   if ((SAVI>0.10 and SAVI< 0.25) and (GDVI >0.30 and GDVI<0.45) ) or
   ((GDVI>0.5) and (SAVI>-0.3 and SAVI<-0.10)) then
5     OutClass = Agriculture
6 if Area is 'Andean highland' then
7   if ((NDWI>-0.20 and NDWI<-0.09) and (VIIRS>10)) or ((NDWI>-0.08 and
   NDWI<0.05)) then
8     OutClass = Built-up
9   if ((NDVI>0.29 and NDVI<0.43)) or (EVI>0.36 and EVI<0.48) or ((SAVI>0.2 and
   SAVI<0.35) ) or ((NDWI>-0.50 and NDWI<-0.30) ) then
10    OutClass = Greenhouse
11  if ((SAVI>0.10 and SAVI<0.25) and (GDVI>0.30 and GDVI<0.45)) then
12    OutClass = Agriculture
13 if Area is 'Amazon' then
14  if ((NDTI<0.19) and (BSI >0 and BSI <0.149) ) or ((UI>-0.05) and (NDBI >-0.13) )
   then
15    OutClass = Built-up
16  if ((SAVI>0.10 and SAVI<0.25) and (GDVI>0.30 and GDVI<0.45)) then
17    OutClass = Agriculture
  
```

3.2. LULC-PBS Maps

The LULC-PBS maps obtained using the proposed methodology are shown in Figure 7. The coast map consists mostly of annual and perennial crops, whereas a small area corresponds to forests. In the Andean highlands, predominant classes are grassland cover and forest, with some patches of annual crops and urban areas identified. The Amazon is dominated by annual and perennial crops, followed by the forest cover type. The best

OA (94.62%) was obtained in the Amazon and the lowest OA (80.2%) was obtained in the coast area. Table 6 shows PA and UA metrics results grouped by ecoregion and the full confusion matrices are reported in Appendix B (Figure A2).

In the coast ecoregion, forests have low PA and high UA which means that not all forest pixels were detected, but in case they are, they actually represented a forest area. Perennial crops have a high PA (91%) and low UA (65%), which indicates that perennial pixel detection on the coast is rather low. The confusion matrix shows that of the 100 pixels corresponding to forests, 42 were classified as perennial crops and 16 as shrubs; see Figure A2a. In the Andean highland target area, the grassland class displays low levels for UA (53.75%). In the corresponding confusion matrix (Figure A2b) some pixels that should have been classified as grassland were classified as annual crops. In Amazon, most LULC-PBS classes obtained high PA and UA values. For instance, the perennial crops had a PA value of 87%, and UA of 100%, i.e., the perennial pixels were identified correctly. Our methodology yielded high F1-Scores for the three target areas: 0.92 for the coast, 0.93 for the Andean highlands, and 1.0 for the Amazon. These scores indicate a high level of accuracy in the classification of the LULC-PBS classes in these ecoregions.

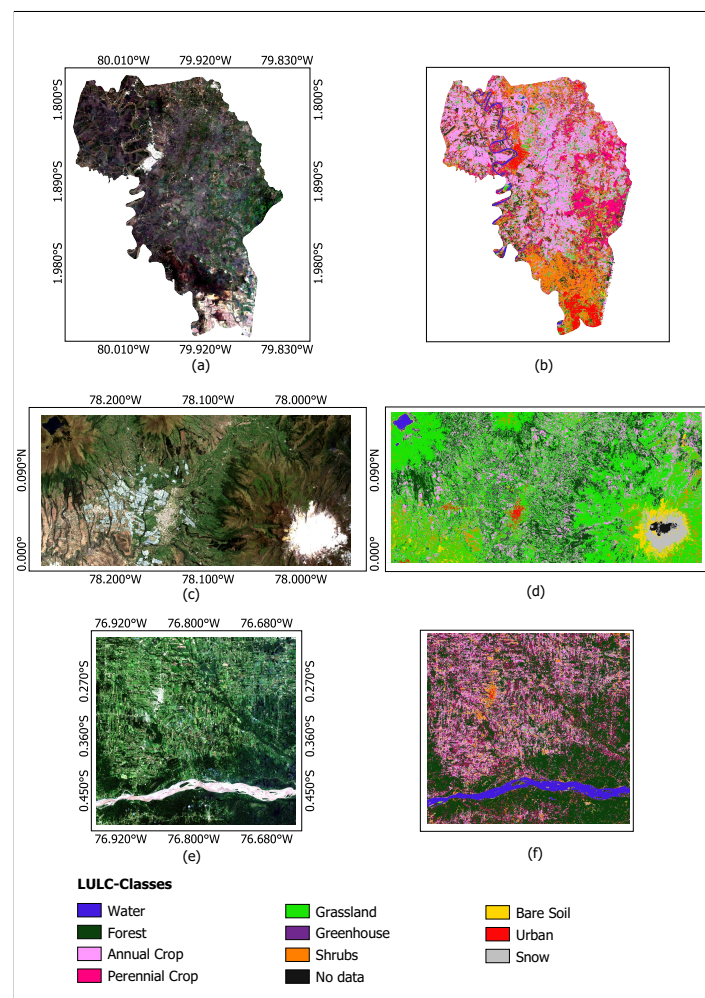


Figure 7. LULC-PBS and RGB Sentinel-2 images of the coast (a,b), Andean highlands (c,d), and Amazon (e,f).

Table 6. Accuracy measures derived from LULC-PBS classification.

Class	Coast		Andean Highland		Amazon	
	PA (%)	UA (%)	PA (%)	UA (%)	PA (%)	UA (%)
Water	99	93.39	86	94.5	100	98.03
Forest	40	75.47	77	78.57	100	84.03
Annual Crop	97	76.98	37	75.51	93	93
Perennial Crop	91	65	-	-	87	100
Greenhouse	-	-	93	95.87	-	-
Grassland	66	79.51	92.07	53.75	70	94.79
Shrub	84	73.04	99	92.52	95	95.95
Bare Soil	65	97.05	70	75.26	94	94.94
Urban area	98	89.08	88	100	97	98.97
Snow	-	-	95	93.13	-	-
OA (%)	80.2		81.9		94.62	
Kappa	0.77		0.79		0.93	
F1-Score	0.92		0.93		1.00	

3.3. Visual Comparison of LULC Maps

Figure 8 shows the sub-areas in DW, Esri-GLC, WC, and LULC-PBS maps and the Google Earth reference image. Below, we discuss the main ambiguities found for each of the following criteria:

- *Dominant Classes:* This occurs when pixels of a given class appear more often than the rest in a map. For instance, urban coverage is observed in most pixels of the reference images of sub-areas A_2^C and A_2^H with some pixels corresponding to bare ground and vegetation. In WC and LULC-PBS maps, most pixels are classified as urban areas while keeping a proportional relationship to the features seen in the corresponding reference image, whereas Esri-GLC and DW maps show a single large urban patch. Similarly, in sub-area A_1^A where an urban area is surrounded by vegetation. Here, vegetation could be interpreted as agricultural mosaics, therefore overestimating the predominant land use class. In sub-area A_1^C , most rivers' pixels in the reference image were labelled as urban areas in Esri-GLC and DW maps, whereas in the WC map, some of them are detected as bare ground. In the LULC-PBS river, pixels were correctly classified as water.
- *Nature-related interclasses conversion:* Natural phenomena may cause temporal changes in land cover and consequently ambiguities in pixel-level classification. This effect can be seen in sub-area A_3^A , in which the reference image shows a river with overbank deposits. These deposits are not detected in WC. LULC-PBS classified them as grassland and both Esri-GLC and DW as bare soil. Similarly, the islet in sub-area A_2^C only appears in WC and LULC-PBS maps.
- *Greenhouses:* These structures usually appear in LULC maps as urban or crops pixels as in sub-areas A_2^H and A_3^H in DW, Esri-GLC and WC maps and as a greenhouse in the proposed LULC-PBS map.
- *Phenological stage transitions:* For example, in A_1^C and A_2^C , a large farmland mosaic in the LULC-PBS map is mapped as grassland in DW and WC products. The Esri-GLC map shows crop areas, although overestimated in size. In the case of sub-area A_3^C , the reference image contains a large area of the Amazonian forest but also a few crop patches. Global products miss these areas that appear in the LULC-PBS map.

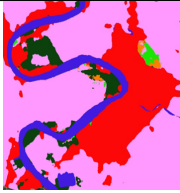
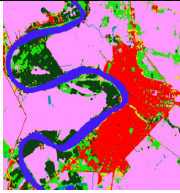
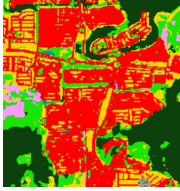
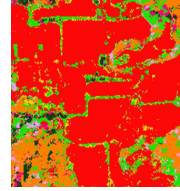
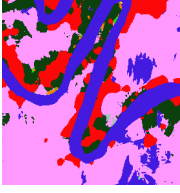
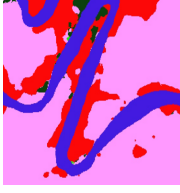
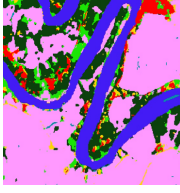
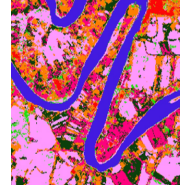
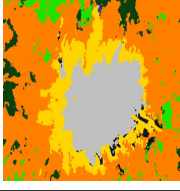
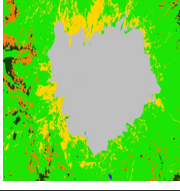
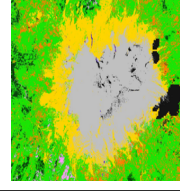
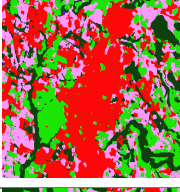
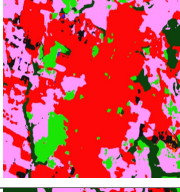
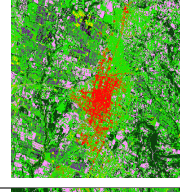
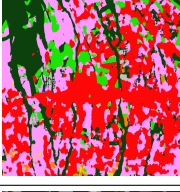
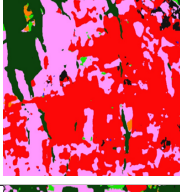
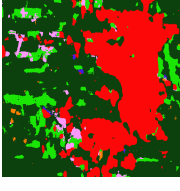
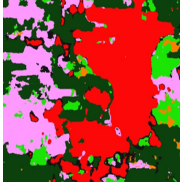
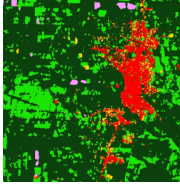
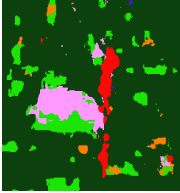
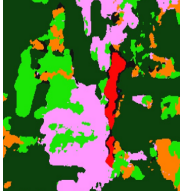
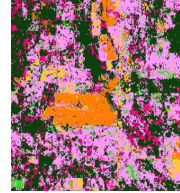
S	Google Earth	DW	Esri-GLC	WC	LULC-PBS
A_1^C					
A_2^C					
A_3^C					
A_1^H					
A_2^H					
A_3^H					
A_1^A					
A_2^A					

Figure 8. Cont.

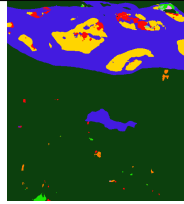
	Google Earth	DW	Esri-GLC	WC	LULC-PBS
A_3^A					
		<ul style="list-style-type: none"> ■ Water ■ Trees ■ Grass ■ Flooded Vegetation ■ Crops ■ Scrub/Shrub ■ Built Area ■ Bare Ground ■ Snow/Ice ■ Clouds 	<ul style="list-style-type: none"> ■ Water ■ Trees ■ Grass ■ Flooded Vegetation ■ Crops ■ Scrub/Shrub ■ Built Area ■ Bare Ground ■ Snow/Ice ■ Clouds 	<ul style="list-style-type: none"> ■ Tree cover ■ Shrubland ■ Grassland ■ Cropland ■ Built-up ■ Bare/ sparse vegetation ■ Snow and Ice ■ Permanent water bodies ■ Herbaceous wetland ■ Mangroves ■ Moss and lichen 	<ul style="list-style-type: none"> ■ Water ■ Forest ■ Annual Crop ■ Perennial Crop ■ Greenhouse ■ Grassland ■ Shrub ■ Bare Soil ■ Urban ■ Snow/Ice ■ Clouds/No Data

Figure 8. Sub-area visual comparison between LULC maps and a high-resolution reference image.

3.4. Surface Area Differences

In Appendix C, we provide additional support for the visual interpretation of the annual variations in the DW, Esri-GLC, and LULC-PBS maps for each of the sub-areas by showing images that illustrate these changes. Furthermore, we computed normalised variation indices for the eight harmonised classes and sub-areas in LULC-PBS (M_1); Esri-GLC (M_2) and Dynamic World (M_3) maps were computed for 2017 to 2020, the year 2017 was used as reference. We found that LULC changes were not consistent across LULC maps as seen in Figure 9, where the percentage of area change is scaled by colour. Results for each sub-area are presented below:

- Coast sub-areas, see Figure 9a:
 - A_1^C : This area is made up of a rural village, crops, and a large river, and therefore showed slight variations in the vegetation, built-up, and water classes. The LULC-PBS map shows a variation of up to 4% in forest (c_{h_2}). LULC-PBS and DW detected changes on surface size from cropland (c_{h_3}) and rangeland (c_{h_4}). Meanwhile, only the DW map showed a variation on water (c_{h_1}), between 2% and 6%.
 - A_2^C : Over the years, this area has changed from agricultural cultivation to urban areas, whereby LULC-PBS and Esri-GLC have correctly detected the variations in the surface area of the built (c_{h_6}) class. Three maps showed variation up to more than 12% in the forest (c_{h_2}), rangeland (c_{h_4}), and bare soil (c_{h_5}) classes.
 - A_3^C : Only two types of land cover changed in size, forest area changed between 2% and 7%, and the cropland between 2% and 4% were detected by LULC-PBS and Esri-GLC.
- Andean highland sub-areas, see Figure 9b:
 - A_1^H : This area contains a volcano with its snow cover surrounded by paramo vegetation; thus, all three maps coincided in detecting changes in the rangeland (c_{h_4}) class. Only the Dynamic world map was able to detect changes up to 14% in the snow (c_{h_7}) class.
 - A_2^H : LULC-PBS and Esri-GLC detected minor variations, up to 2%, in forest (c_{h_2}) and rangeland (c_{h_4}) classes. The cropland class (c_{h_3}) showed a change in the area up to 14% in all three maps. A_3^H : forest (c_{h_2}) and cropland (c_{h_3}) classes varied in size, by about 6% in LULC-PBS and Esri-GLC, respectively. Rangeland (c_{h_4}) varied by more than 14% in the PBS-LULC map only.
- Amazon sub-areas, see Figure 9c:

A_1^A : It is a small village area surrounded by forest and crops. All three maps detected dynamism among the classes corresponding to vegetation. LULC-PBS was the only map that did not detect any changes in the built (c_{h_6}) class.

A_2^A : It is an area covered with crops. All three maps showed changes of up to 12% in vegetation classes. Meanwhile, the Dynamic world map did not detect any changes in the bare soil (c_{h_5}) class.

A_3^A : This area shows a large forest with patches of cropland. Only LULC-PBS was able to detect variations in the forest (c_{h_2}) and cropland (c_{h_3}) classes changed from 2% to 4%. Visual analysis of the study area revealed the presence of a river containing several islets. Our results showed that the Esri-GLC and DW maps indicated changes ranging from 6% to 8% in the bare soil (c_{h_5}) class, whereas all three maps showed changes in the water (c_{h_1}) class.

The three maps showed changes in water (c_{h_1}).

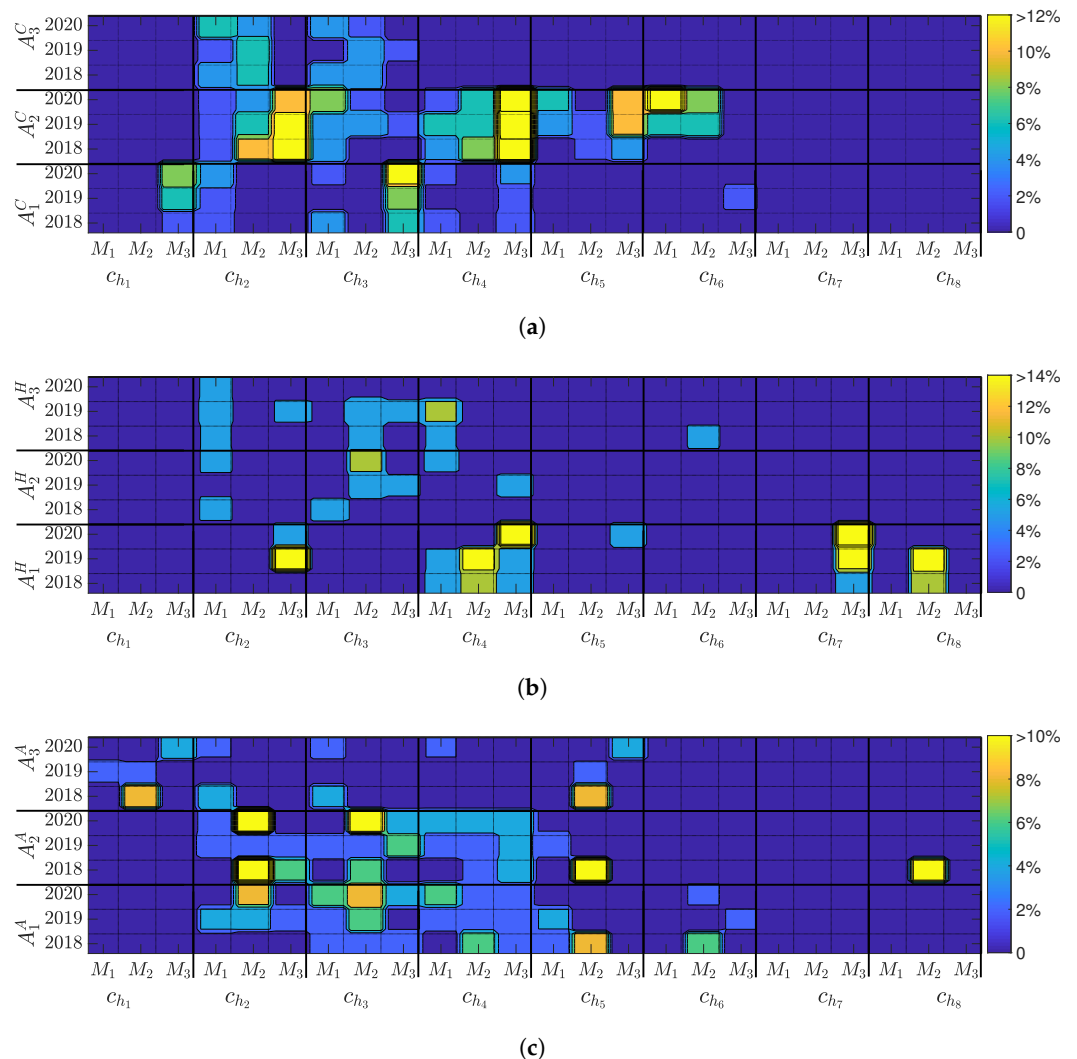


Figure 9. Annual variation comparison of LULC-PBS (M_1), Esri-GLC (M_2), and Dynamic World (M_3) on sub-areas extracted from the (a) coast, (b) Andean highland, and (c) Amazon target areas.

4. Discussion

The proposed methodology proved useful to capture LULC dynamics in complex and heterogeneous regions of Ecuador. Our LULC-PBS map not only displays high classification accuracy but also spatial consistency with commercially available global LULC products.

4.1. PBS Classification

We noted that classification accuracy rates decrease in areas with high land cover dynamics. For instance, forest and perennial crop classes in the coast target area report the lowest detection accuracy because the reflectance values of different species of fruit trees and forest trees can be similar, leading to misclassification.

For annual crops and urban zones, our map obtained high accuracy values in all sub-areas. Annual crop detection was achieved due to class separability analysis using spectral indices. For urban class accuracy, in addition to the spectral indices, the VIIRS (DNB) dataset was used to improve the classification accuracy, as reported in [61], where it was shown that the inclusion of VIIRS (DNB) contributes to improving the accuracy of the results in the urban area identification. On the other hand, LULC-PBS maps were generated for the years 2017 to 2020 for the comparison study with the global products.

The ten LULC classes in our map are not only useful for understanding land surface processes, but they also improve the information available for biodiversity studies. For example, the forest, grassland, and shrubs classes are vegetation, which plays a key role in improving ecosystem performance [62]. The transition from the vegetation class to the bare soil class is useful for understanding the status and monitoring of desertification or deforestation [63]. The snow class in the paramo helps to quantify snowmelt in the Andes [64]. The information from the urban class can enable the monitoring of urbanisation and settlement pattern [65] and provide a large-scale base layer for the more detailed mapping of local climatological zones in urban areas [66], which are the focus of many studies. Moreover, the combination of the urban and vegetation class in the city could be exploited to assess the impacts of urban form on the landscape structure of urban green spaces. In addition to these ecological benefits, our methodology can also be used to identify areas where indigenous communities may be impacted by LULC changes. By enabling further research on the interactions between indigenous communities and LULC dynamics observed in this study, we can identify opportunities to mitigate negative impacts and support community-based conservation efforts.

4.2. Global Product Comparison

Our results show that urban class is overestimated in both the WC and Esri-GLC maps. In fact, many water pixels were misclassified as built-up. To cope with this effect, Ref. [67] suggested that the global products should use night light data to improve classification accuracy in the urban area, as in the LULC-PBS map. On the other hand, although the water class was the most accurate in the global products [68], our study revealed that the water class was not correctly represented by these products in the evaluated areas.

We highlight that there is confusion in the classification of LULC products due to the fact that some areas are affected by temporary natural phenomena, e.g., in rivers when in the dry season the flow decreases and sediments are formed. This misclassification depends on the number of observations obtained for each different season.

As for greenhouses, our map identified them as croplands, whereas the global products identified them as urban. This is explained by the fact that greenhouses are made of artificial materials and therefore DW, Esri-GLC, and WC, which are only land cover maps, classify them as built-up areas. Our proposed map also considered land use classes and therefore classified them as greenhouses.

Moreover, we found that the global products showed inaccuracies in classifying crop areas, and in some cases, these were classified as grassland or shrubland, which may occur due to the dates of acquisition of the images on the phenological cycle of the crops.

On the other hand, LULC maps must reflect the dynamism of the landscape, so we focused on the variations of the products available on an annual basis. However, only Esri-GLC and LULC-PBS showed variations in urban class within the sub-area A_2^C . DW could not detect any urban area changes in the period from 2017 to 2020, despite this sub-area having been characterised by rapid urban expansion in recent years [69,70].

In sub-area A_3^A , LULC-PBS showed variations and was even the only LULC product to identify cropland classes within this sub-area in 2020 (see Figure 8), whereas the global products showed no variation in their vegetation classes such as forest, cropland and rangeland. However, Refs. [71–73] reported that the area assessed has suffered from deforestation in recent years.

Thus, the differences and discrepancies in accuracy found between global and LULC-PBS products are due to the different biogeographical conditions, which generate different spectral signatures within the same LULC class.

4.3. Limitations

Although our product, LULC-PBS, achieved high overall classification accuracy, we also found shortcomings among its LULC classes. We detected limitations in the quality and quantity of the image collection as we used a phenology-based algorithm which required capturing the state of all phenological stages of vegetation. Furthermore, cloud contamination reduced the quality of the images captured through the optical sensors, causing them to be discarded for the phenology-based algorithm, and thus leading to misclassification. Another limitation is that the training data were acquired by visual interpretation. Therefore, SDC threshold values are not entirely reliable. However, to improve threshold values further, research could focus on developing approaches for automatically detecting optimal threshold values for the different indices used in our algorithm, such as machine learning algorithms, decision trees, or support vector machines, to automatically learn the best threshold values from the training data. Another approach is the use of clustering techniques, such as k-means or fuzzy clustering, to group pixels with similar spectral properties and identify threshold values based on these groups.

5. Conclusions and Recommendations

The timely mapping of complex and heterogeneous landscapes is necessary to understand the dynamics of LULC changes. This study had two main focuses: (i) to provide a regional-scale LULC product that includes dynamic landscape areas at 10 m spatial resolution using the powerful free cloud-based software tool, GEE; (ii) to compare LULC-PBS with existing global products within the three target study areas.

Firstly, using GEE, we generated LULC maps in three distinct Ecuadorian ecoregions, with a ground sampling distance (GSD) of 10 m. Our adapted methodology allowed us not only to identify land cover classes but also to map land use classes, such as agriculture and urban areas, using phenology-based algorithms and data from multiple sources. The proposed methodology provided reasonable performance with an overall accuracy between 80.2% and 97.12% depending on the conditions of the ecoregions.

By adding very few extra reference pixels, the global PBS approach was fine-tuned to work at the regional scale. Hence, this approach has the potential for regional mapping, as long as it is well-calibrated. In this sense, our research findings are able to contribute to the current knowledge of LULC classification. Moreover, the present results were obtained using accessible optical data computed on a cloud-based platform considering our study area. In tropical regions, obtaining long-term optical data can be challenging; thus, it is crucial to explore the potential of Synthetic Aperture Radar (SAR) data for future work. Therefore, we encourage the combined use of Sentinel-1 and Sentinel-2 for LULC classification, considering the availability of observations.

Secondly, in our comparative results between the global LULC and LULC-PBS maps, we found inaccuracies and spatial discrepancies in each product that vary between the different ecoregions. In the visual comparison of the LULC products with the Google Earth image, we found that LULC-PBS showed a consistent spatial representation, followed by the global WC product, which showed urban areas correctly identified. LULC-PBS showed yearly variations in classes and areas that maintain high dynamism. Although Esri-GLC showed changes in the urban class, it also showed an overestimation of the urban class. Therefore, global products have limitations and biases at the regional level. We suggest that

when using global LULC products, the purpose of their application should be considered, as these maps tend to show some deficiencies when they are used independently in specific areas. However, global products can be integrated with local datasets to improve the accuracy of local LULC maps [26].

In conclusion, this study provides a glimpse of the inconsistencies of global products when applied in a regional context, which could affect decision-making on environmental conservation or sustainability. In addition, we provide a solution to map LULC at the regional level through a phenological approach algorithm that could be adopted in the future to map national LULC with an annual frequency and a finer resolution. Furthermore, this methodology can be used for national mapping in South American countries with ecoregions similar to those evaluated in this work.

Author Contributions: Conceptualisation, G.V.R.; methodology, G.V.R., D.O. and F.V.C.; software, G.V.R.; formal analysis, G.V.R. and J.M.M.; investigation, G.V.R.; data curation, G.V.R.; writing—original draft preparation, G.V.R.; writing—review and editing, G.V.R., F.V.C. and D.O.; visualisation, G.V.R.; supervision, F.V.C.; project administration, F.V.C.; funding acquisition, G.V.R. All authors have read and agreed to the published version of the manuscript.

Funding: The work of G. Villegas was supported by Secretaría Nacional de Educación Superior, Ciencia, Tecnología e Innovación (SENESCYT) under the funding number ARSEQ-BEC-002773-2017.

Data Availability Statement: The GEE scripts are available on the following GitHub page: <https://github.com/eosGV/LULC-PBS> (accessed on 14 April 2023).

Acknowledgments: We are grateful that the Google Earth Engine provides computational capacities. We also thank ESA for sharing Sentinel-2 data.

Conflicts of Interest: The authors declare no conflict of interest. The funders had no role in the design of the study; in the collection, analyses or interpretation of data; in the writing of the manuscript or in the decision to publish the results.

Appendix A. Monthly Spectral Index

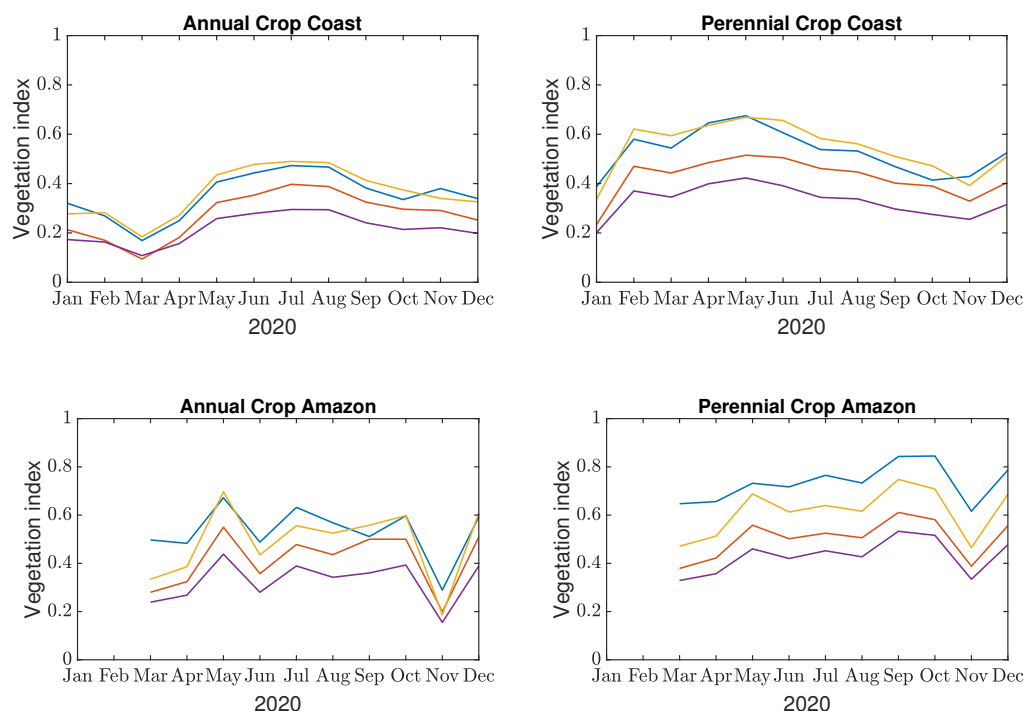


Figure A1. Cont.

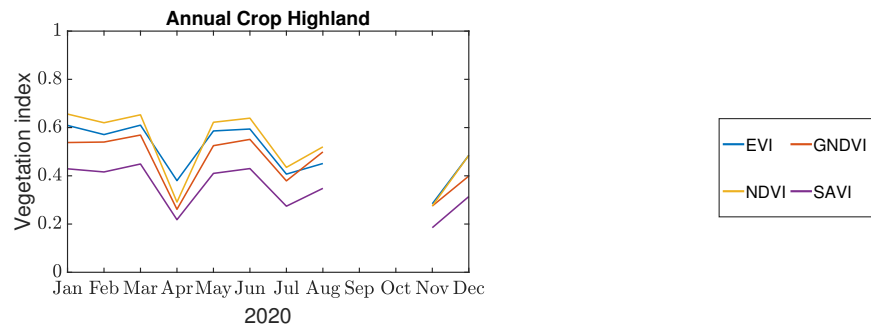


Figure A1. Monthly spectral index profiles of annual and perennial crops 2020.

Appendix B. Confusion Matrices

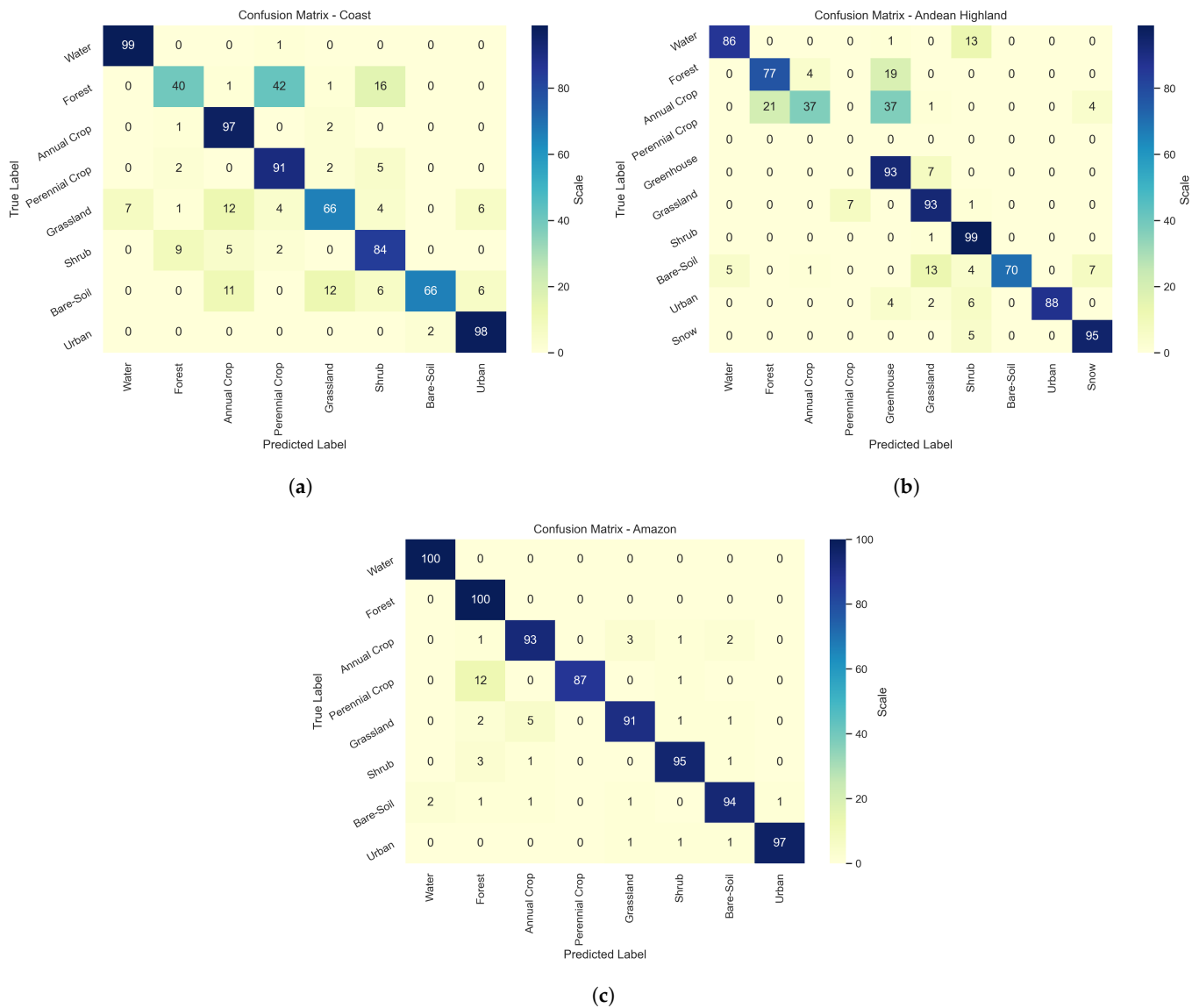


Figure A2. The confusion matrices obtained from different target areas: (a) coast, (b) Andean highland, and (c) Amazon.

Appendix C. Annual Visual Comparison between Different Land Cover Products in Ecuadorian Ecoregions

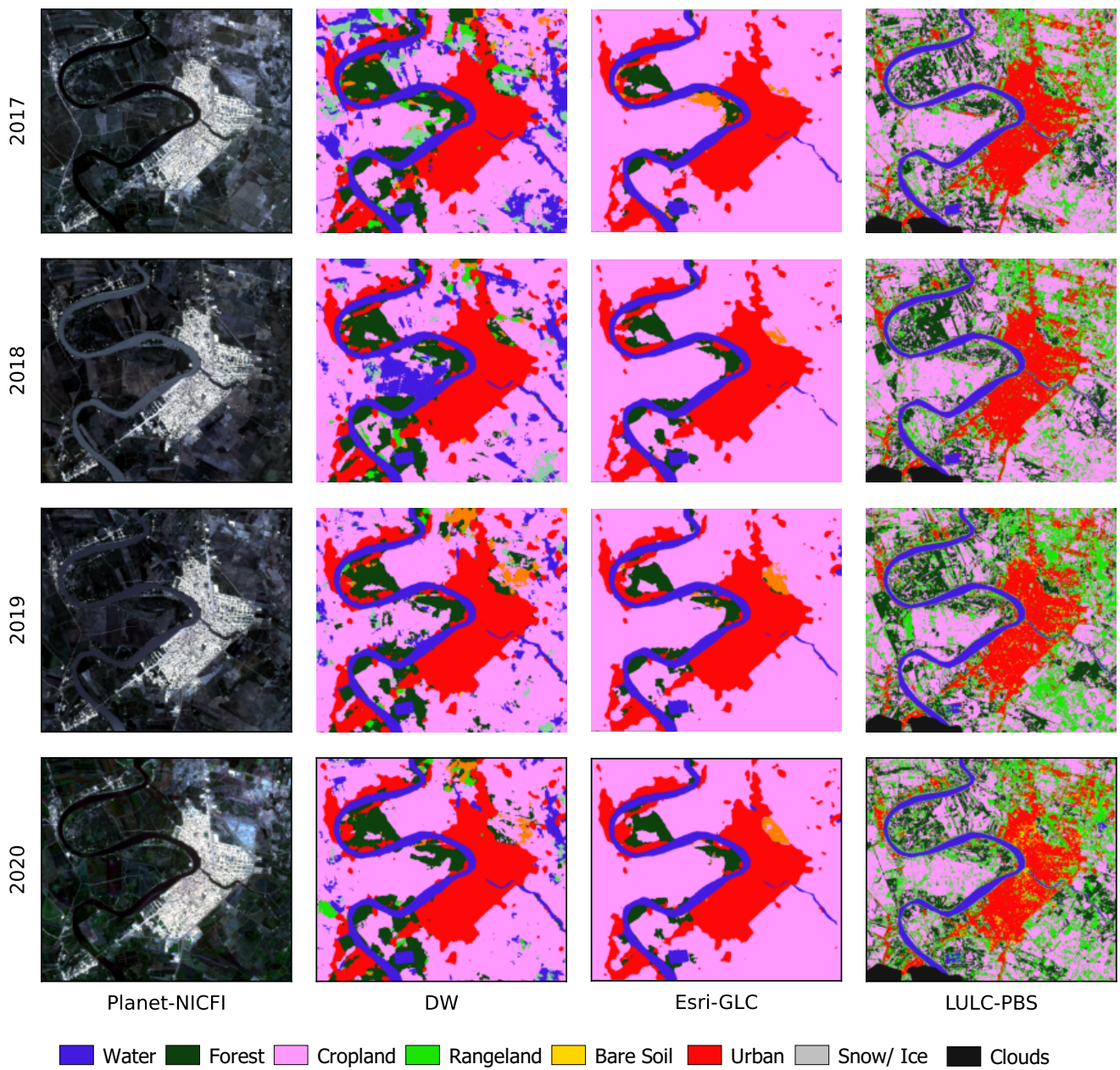


Figure A3. Annual spatial comparison between DW, Esri-GLC, and LULC-PBS maps in the coast ecoregion, site A_1^C .

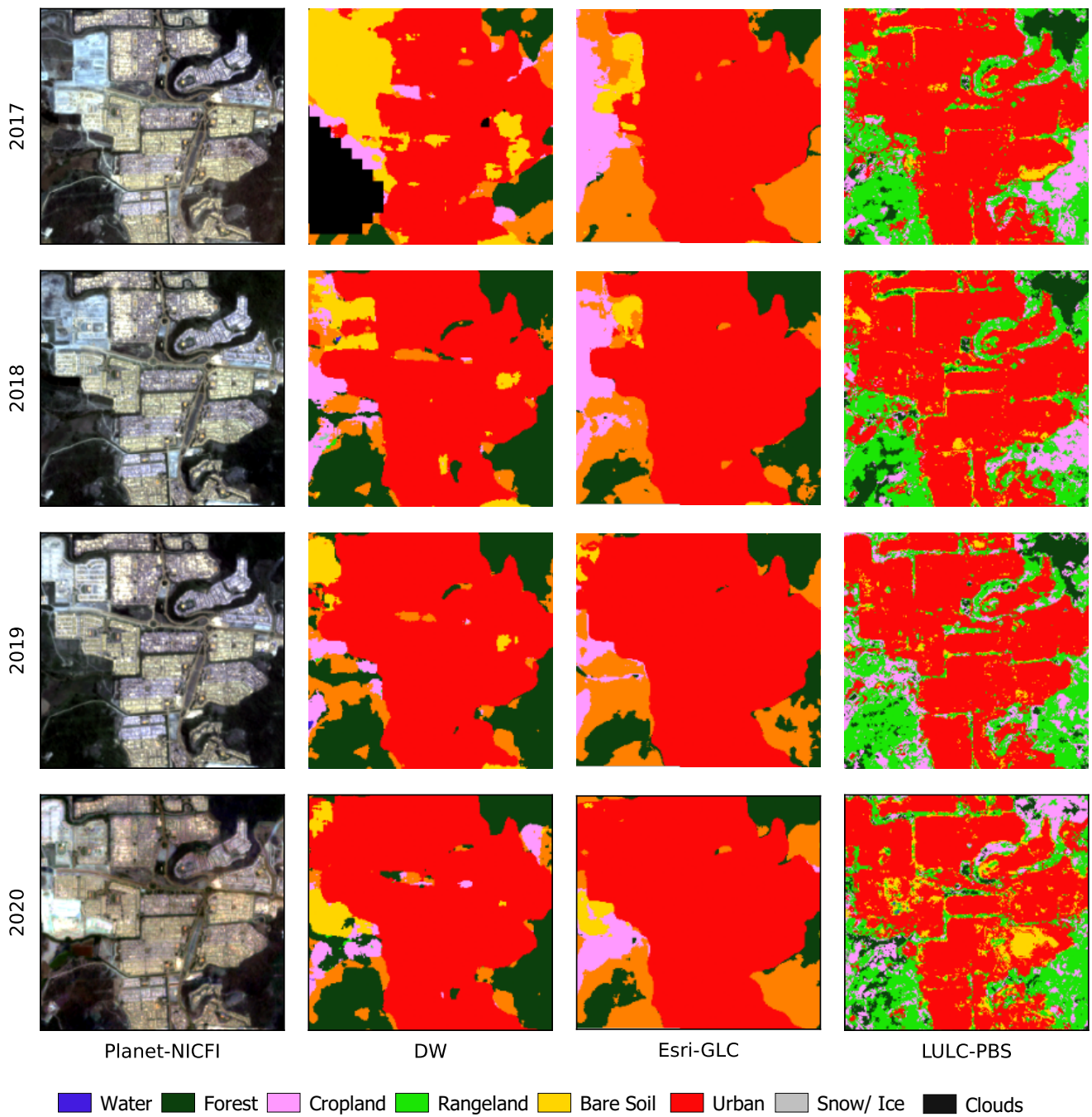


Figure A4. Annual spatial comparison between DW, Esri-GLC, and LULC-PBS maps in the coast ecoregion, site A_2^C .

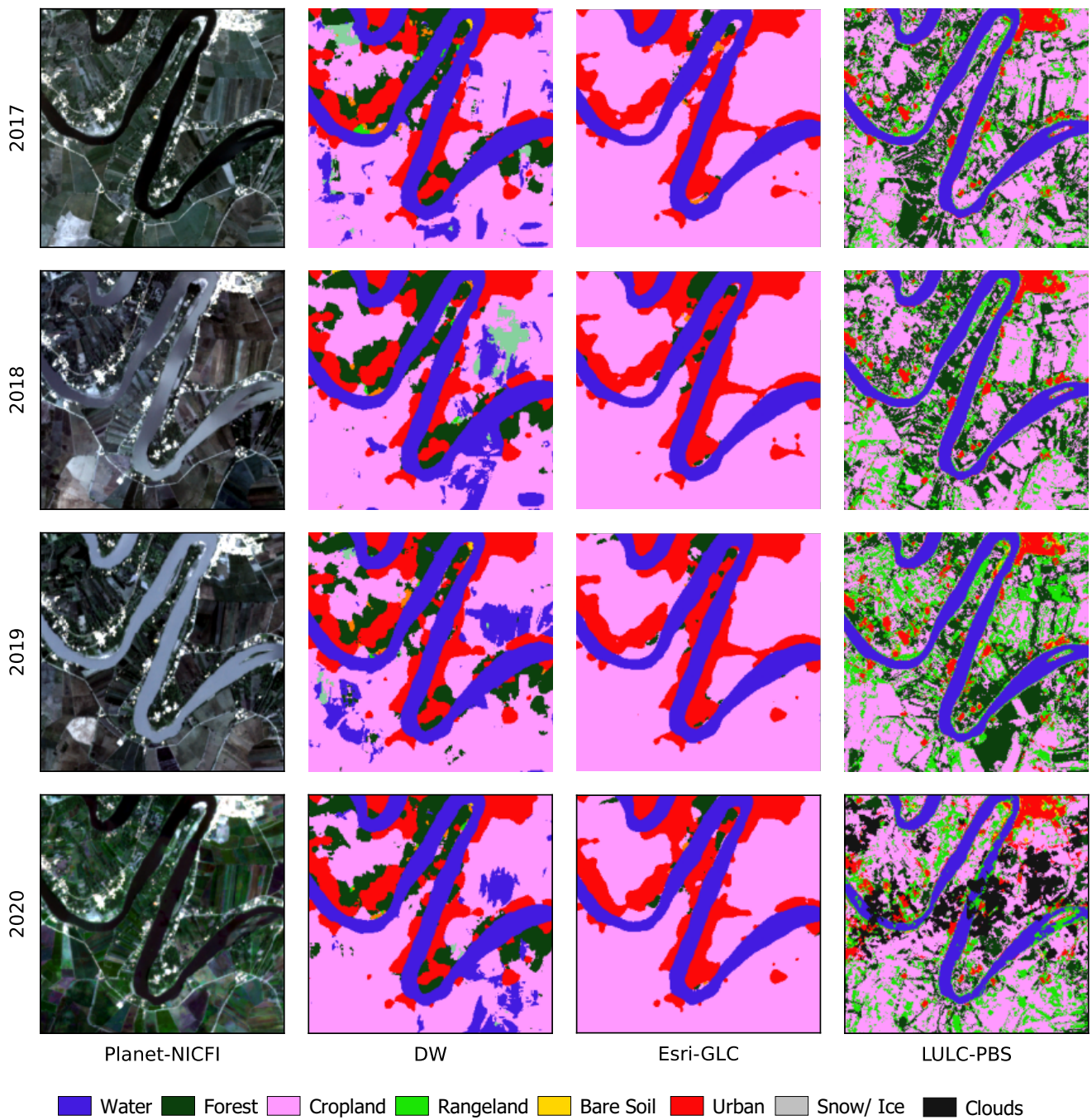


Figure A5. Annual spatial comparison between DW, Esri-GLC, and LULC-PBS maps in the coast ecoregion, site A_3^C .

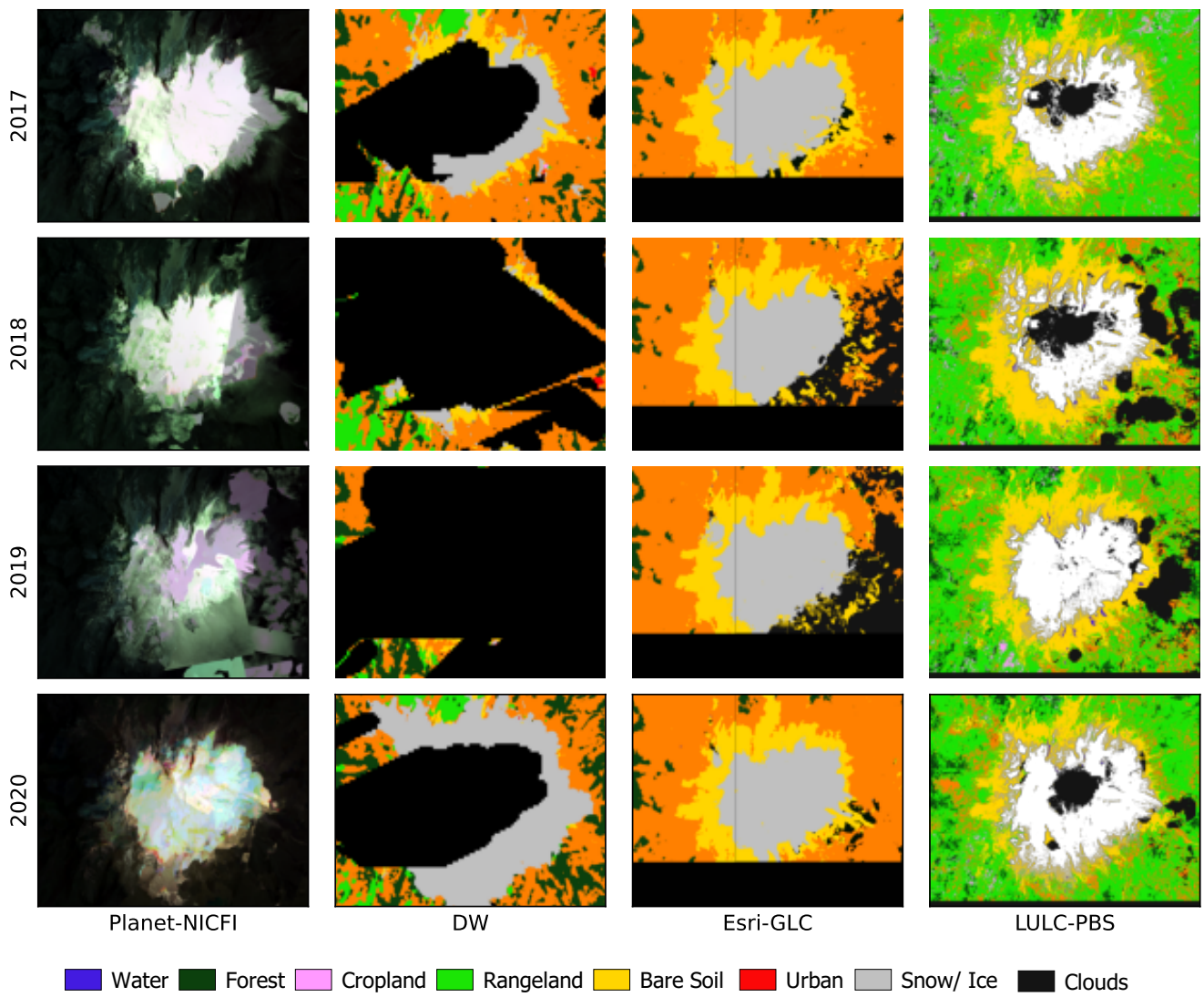


Figure A6. Annual spatial comparison between DW, Esri-GLC, and LULC-PBS maps in the Andean highland ecoregion, site A_1^H .

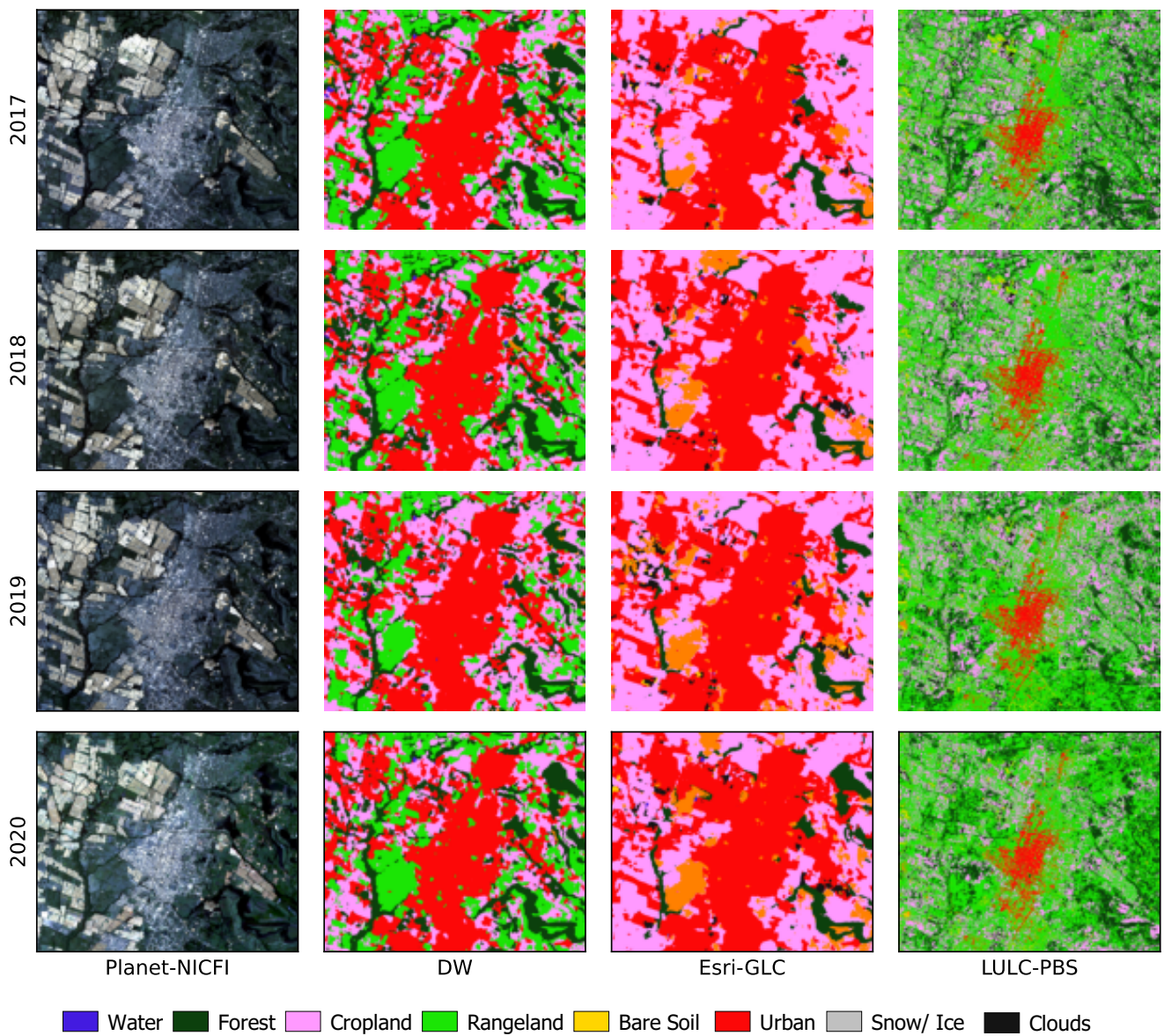


Figure A7. Annual spatial comparison between DW, Esri-GLC, and LULC-PBS maps in the Andean highland ecoregion, site A_2^H .

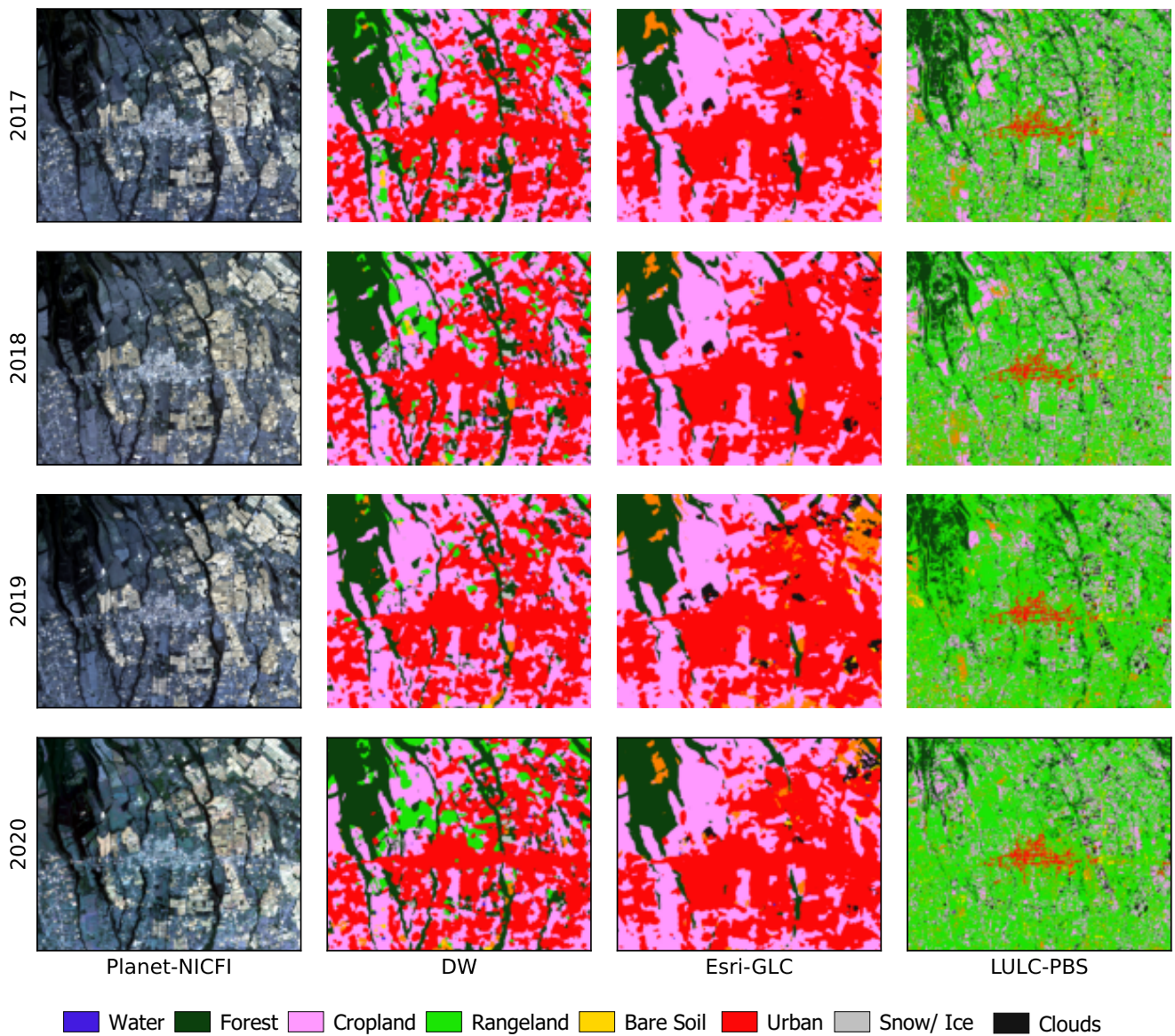


Figure A8. Annual spatial comparison between DW, Esri-GLC, and LULC-PBS maps in the Andean highland ecoregion, site A_3^H .

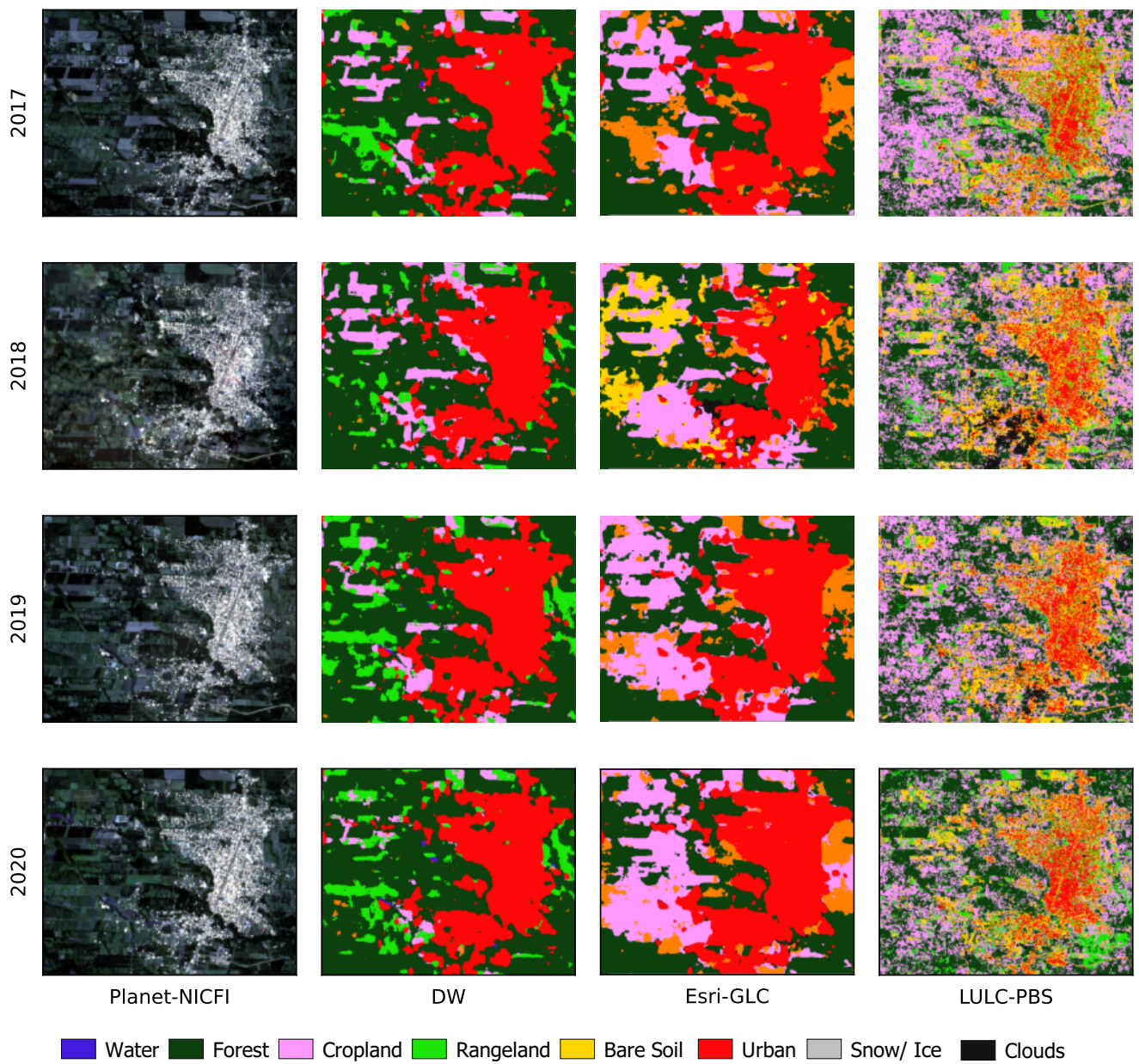


Figure A9. Annual spatial comparison between DW, Esri-GLC, and LULC-PBS maps in the Amazon ecoregion, site A_1^A .

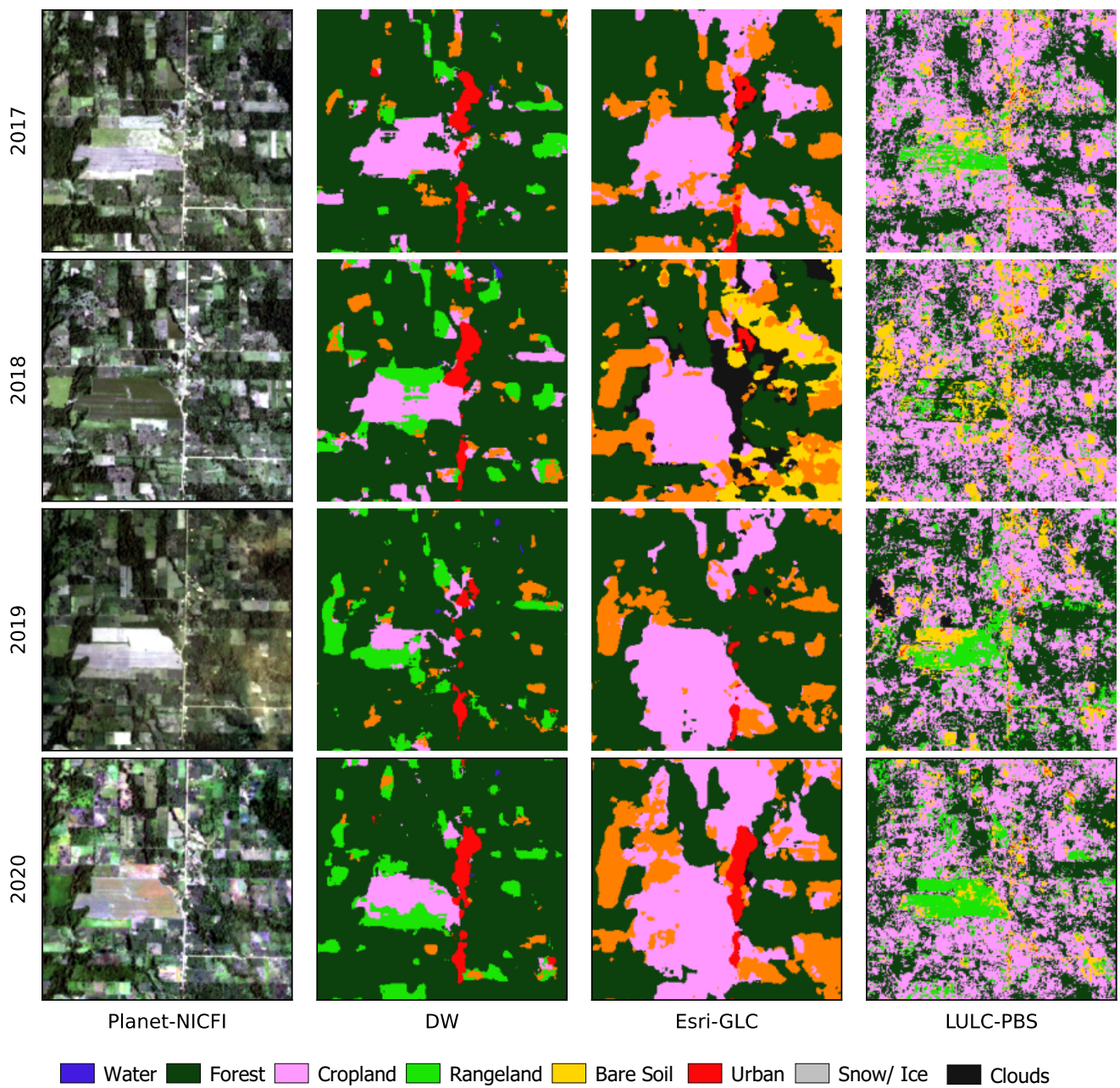


Figure A10. Annual spatial comparison between DW, Esri-GLC, and LULC-PBS maps in the Amazon ecoregion, site A_2^A .

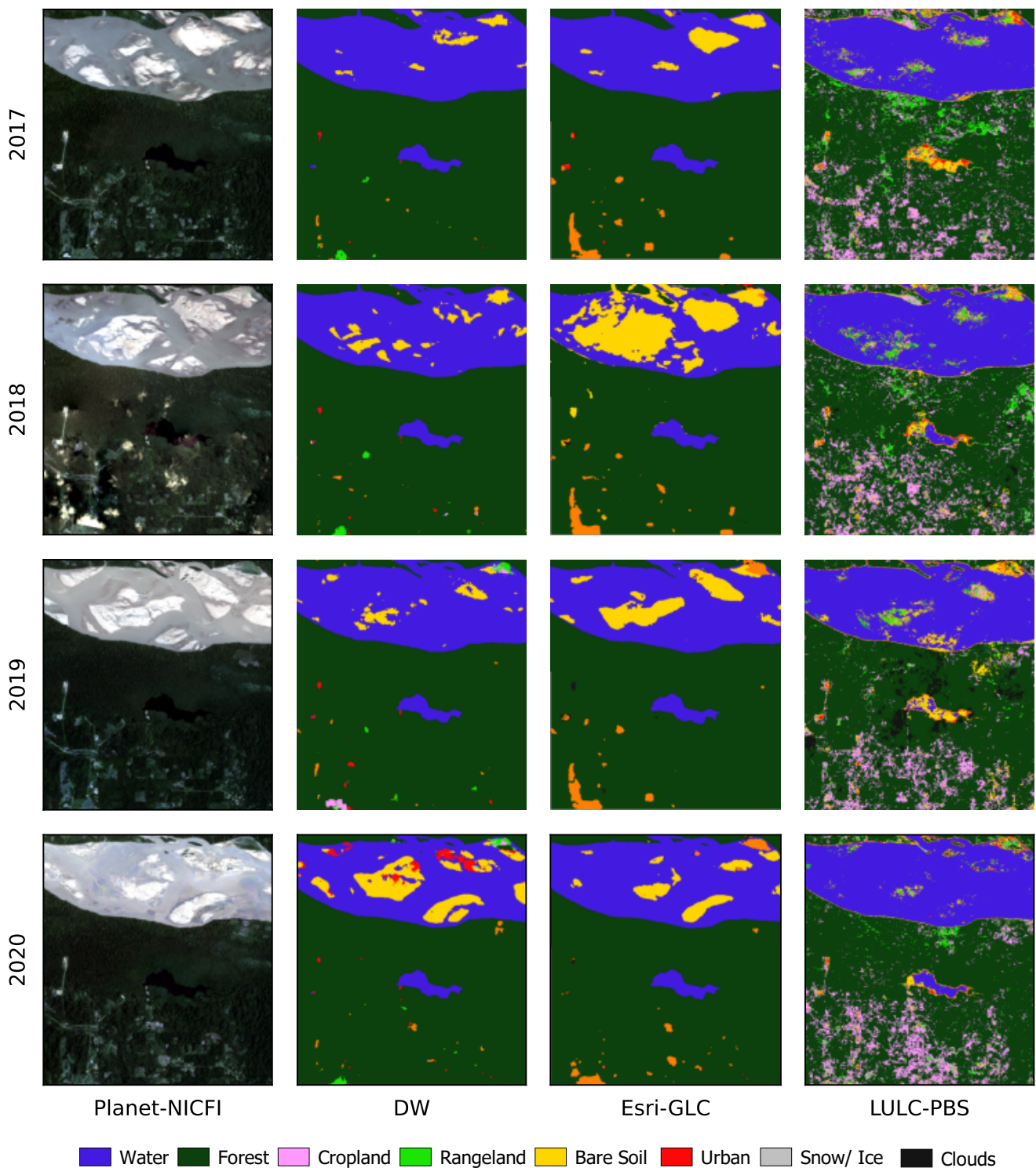


Figure A11. Annual spatial comparison between DW, Esri-GLC, and LULC-PBS maps in the Amazon ecoregion, site A_3^A .

References

1. Talukdar, S.; Singha, P.; Mahato, S.; Pal, S.; Liou, Y.A.; Rahman, A. Land-use land-cover classification by machine learning classifiers for satellite observations—A review. *Remote Sens.* **2020**, *12*, 1135. [[CrossRef](#)]
2. Ngondo, J.; Mango, J.; Liu, R.; Nobert, J.; Dubi, A.; Cheng, H. Land-use and land-cover (LULC) change detection and the implications for coastal water resource management in the Wami–Ruvu Basin, Tanzania. *Sustainability* **2021**, *13*, 4092. [[CrossRef](#)]

3. Hansen, M.C.; DeFries, R.S.; Townshend, J.R.; Sohlberg, R. Global land cover classification at 1 km spatial resolution using a classification tree approach. *Int. J. Remote Sens.* **2000**, *21*, 1331–1364. [[CrossRef](#)]
4. Loveland, T.R.; Reed, B.C.; Brown, J.F.; Ohlen, D.O.; Zhu, Z.; Yang, L.; Merchant, J.W. Development of a global land cover characteristics database and IGBP DISCover from 1 km AVHRR data. *Int. J. Remote Sens.* **2000**, *21*, 1303–1330. [[CrossRef](#)]
5. Friedl, M.A.; Sulla-Menashe, D.; Tan, B.; Schneider, A.; Ramankutty, N.; Sibley, A.; Huang, X. MODIS Collection 5 global land cover: Algorithm refinements and characterization of new datasets. *Remote Sens. Environ.* **2010**, *114*, 168–182. [[CrossRef](#)]
6. Bicheron, P.; Leroy, M.; Brockmann, C.; Krämer, U.; Miras, B.; Huc, M.; Ninõ, F.; Defourny, P.; Vancutsem, C.; Arino, O.; et al. GLOBCOVER: A 300 m global land cover product for 2005 using ENVISAT MERIS time series. In Proceedings of the Recent Advances in Quantitative Remote Sensing Symposium, Torrent, Spain, 25–29 September 2006; pp. 538–542.
7. Karra, K.; Kontgis, C.; Statman-Weil, Z.; Mazzariello, J.C.; Mathis, M.; Brumby, S.P. Global land use/land cover with Sentinel-2 and deep learning. In Proceedings of the IGARSS 2021–2021 IEEE International Geoscience and Remote Sensing Symposium, Brussels, Belgium, 11–16 July 2021.
8. Zanaga, D.; Van De Kerchove, R.; De Keersmaecker, W.; Souverijns, N.; Brockmann, C.; Quast, R.; Wevers, J.; Grosu, A.; Paccini, A.; Vergnaud, S.; et al. ESA WorldCover 10 m 2020 v100. 2021. Available online: https://developers.google.com/earth-engine/datasets/catalog/ESA_WorldCover_v100#description (accessed on 10 January 2021).
9. Brown, C.F.; Brumby, S.P.; Guzder-Williams, B.; Birch, T.; Hyde, S.B.; Mazzariello, J.; Czerwinski, W.; Pasquarella, V.J.; Haertel, R.; Ilyushchenko, S.; et al. Dynamic World, Near real-time global 10 m land use land cover mapping. *Sci. Data* **2022**, *9*, 251. [[CrossRef](#)]
10. Chaaban, F.; El Khattabi, J.; Darwishe, H. Accuracy Assessment of ESA WorldCover 2020 and ESRI 2020 Land Cover Maps for a Region in Syria. *J. Geovis. Spat. Anal.* **2022**, *6*, 31. [[CrossRef](#)]
11. Wang, J.; Yang, X.; Wang, Z.; Cheng, H.; Kang, J.; Tang, H.; Li, Y.; Bian, Z.; Bai, Z. Consistency Analysis and Accuracy Assessment of Three Global Ten-Meter Land Cover Products in Rocky Desertification Region—A Case Study of Southwest China. *Isprs Int. J. Geo-Inf.* **2022**, *11*, 202. [[CrossRef](#)]
12. Pandey, P.C.; Koutsias, N.; Petropoulos, G.P.; Srivastava, P.K.; Ben Dor, E. Land use/land cover in view of earth observation: Data sources, input dimensions, and classifiers—A review of the state of the art. *Geocarto Int.* **2021**, *36*, 957–988. [[CrossRef](#)]
13. Alshari, E.A.; Gawali, B.W. Development of classification system for LULC using remote sensing and GIS. *Glob. Transitions Proc.* **2021**, *2*, 8–17. [[CrossRef](#)]
14. Omeer, A.A.; Deshmukh, R.R.; Gupta, R.S.; Kayte, J.N. Land Use and Cover Mapping Using SVM and MLC Classifiers: A Case Study of Aurangabad City, Maharashtra, India. In Proceedings of the International Conference on Recent Trends in Image Processing and Pattern Recognition, Solapur, India, 21–22 December 2018; Springer: Berlin/Heidelberg, Germany, 2018; pp. 482–492. [[CrossRef](#)]
15. Loukika, K.N.; Keesara, V.R.; Sridhar, V. Analysis of Land Use and Land Cover Using Machine Learning Algorithms on Google Earth Engine for Munneru River Basin, India. *Sustainability* **2021**, *13*, 13758. [[CrossRef](#)]
16. Varade, D.; Sure, A.; Dikshit, O. Potential of Landsat-8 and Sentinel-2A composite for land use land cover analysis. *Geocarto Int.* **2019**, *34*, 1552–1567. [[CrossRef](#)]
17. Khan, A.; Govil, H.; Kumar, G.; Dave, R. Synergistic use of Sentinel-1 and Sentinel-2 for improved LULC mapping with special reference to bad land class: A case study for Yamuna River floodplain, India. *Spat. Inf. Res.* **2020**, *28*, 669–681. [[CrossRef](#)]
18. Sánchez-Espinosa, A.; Schröder, C. Land use and land cover mapping in wetlands one step closer to the ground: Sentinel-2 versus landsat 8. *J. Environ. Manag.* **2019**, *247*, 484–498. [[CrossRef](#)]
19. Yan, E.; Wang, G.; Lin, H.; Xia, C.; Sun, H. Phenology-based classification of vegetation cover types in Northeast China using MODIS NDVI and EVI time series. *Int. J. Remote Sens.* **2015**, *36*, 489–512. [[CrossRef](#)]
20. Htitiou, A.; Boudhar, A.; Lebrini, Y.; Hadria, R.; Lionboui, H.; Elmansouri, L.; Tychon, B.; Benabdelouahab, T. The performance of random forest classification based on phenological metrics derived from Sentinel-2 and Landsat 8 to map crop cover in an irrigated semi-arid region. *Remote Sens. Earth Syst. Sci.* **2019**, *2*, 208–224. [[CrossRef](#)]
21. Kpienbaareh, D.; Sun, X.; Wang, J.; Luginaah, I.; Bezner Kerr, R.; Lupafya, E.; Dakishoni, L. Crop type and land cover mapping in northern Malawi using the integration of sentinel-1, sentinel-2, and planetscope satellite data. *Remote Sens.* **2021**, *13*, 700. [[CrossRef](#)]
22. Solórzano, J.V.; Mas, J.F.; Gao, Y.; Gallardo-Cruz, J.A. Land use land cover classification with U-net: Advantages of combining sentinel-1 and sentinel-2 imagery. *Remote Sens.* **2021**, *13*, 3600. [[CrossRef](#)]
23. Zhang, X.y.; Feng, X.z.; Deng, H. Land-cover density-based approach to urban land use mapping using high-resolution imagery. *Chin. Geogr. Sci.* **2005**, *15*, 162–167. [[CrossRef](#)]
24. Zhang, Y.; Li, Q.; Huang, H.; Wu, W.; Du, X.; Wang, H. The combined use of remote sensing and social sensing data in fine-grained urban land use mapping: A case study in Beijing, China. *Remote Sens.* **2017**, *9*, 865. [[CrossRef](#)]
25. Johnson, B.A.; Iizuka, K. Integrating OpenStreetMap crowdsourced data and Landsat time-series imagery for rapid land use/land cover (LULC) mapping: Case study of the Laguna de Bay area of the Philippines. *Appl. Geogr.* **2016**, *67*, 140–149. [[CrossRef](#)]
26. Huan, V. Accuracy assessment of land use land cover LULC 2020 (ESRI) data in Con Dao island, Ba Ria–Vung Tau province, Vietnam. In Proceedings of the IOP Conference Series: Earth and Environmental Science, Virtual, 28–29 December 2022; IOP Publishing: Bristol, UK, 2022; Volume 1028, p. 012010.

27. Liu, X.; He, J.; Yao, Y.; Zhang, J.; Liang, H.; Wang, H.; Hong, Y. Classifying urban land use by integrating remote sensing and social media data. *Int. J. Geogr. Inf. Sci.* **2017**, *31*, 1675–1696. [[CrossRef](#)]
28. Jia, Y.; Ge, Y.; Ling, F.; Guo, X.; Wang, J.; Wang, L.; Chen, Y.; Li, X. Urban land use mapping by combining remote sensing imagery and mobile phone positioning data. *Remote Sens.* **2018**, *10*, 446. [[CrossRef](#)]
29. Yonaba, R.; Koita, M.; Mounirou, L.; Tazen, F.; Queloz, P.; Biaou, A.; Niang, D.; Zouré, C.; Karambiri, H.; Yacouba, H. Spatial and transient modelling of land use/land cover (LULC) dynamics in a Sahelian landscape under semi-arid climate in northern Burkina Faso. *Land Use Policy* **2021**, *103*, 105305. [[CrossRef](#)]
30. Zhao, Y.; Feng, D.; Yu, L.; Wang, X.; Chen, Y.; Bai, Y.; Hernández, H.J.; Galleguillos, M.; Estades, C.; Biging, G.S.; et al. Detailed dynamic land cover mapping of Chile: Accuracy improvement by integrating multi-temporal data. *Remote Sens. Environ.* **2016**, *183*, 170–185. [[CrossRef](#)]
31. Mapa de Precipitación Media Multianual. 1965–1999. Available online: https://www.inamhi.gob.ec/docum_institucion/MapasBiblioteca/5%20PrecipitacionA0.pdf (accessed on 5 March 2020).
32. Plan de Desarrollo y Ordenamiento Territorial del Cantón Daule 2015–2025. 2015. Available online: https://www.daule.gob.ec/documentos/20124/39854/PDOT_DAULE_2015-2025.pdf (accessed on 10 January 2021).
33. Hribljan, J.A.; Suárez, E.; Heckman, K.A.; Lilleskov, E.A.; Chimner, R.A. Peatland carbon stocks and accumulation rates in the Ecuadorian páramo. *Weil. Ecol. Manag.* **2016**, *24*, 113–127. [[CrossRef](#)]
34. Pitman, N.C.A. *A Large-Scale Inventory of Two Amazonian Tree Communities*; Duke University: Durham, NC, USA, 2000.
35. Plan de Desarrollo y Ordenamiento Territorial de la Provincia de Orellana 2015–2019. 2015. Available online: https://www.gporellana.gob.ec/wp-content/uploads/2015/11/PDYOT-2015-2019_ORELLANA_ACTUALIZADO.pdf (accessed on 10 January 2021).
36. Small, C. Multisensor characterization of urban morphology and network structure. *Remote Sens.* **2019**, *11*, 2162. [[CrossRef](#)]
37. Liu, Z.; Zhang, Q.; Yue, D.; Hao, Y.; Su, K. Extraction of urban built-up areas based on Sentinel-2A and NPP-VIIRS nighttime light data. *Remote Sens. Land Resour.* **2019**, *4*, 227–234.
38. Song, Y.; Chen, B.; Kwan, M.P. How does urban expansion impact people’s exposure to green environments? A comparative study of 290 Chinese cities. *J. Clean. Prod.* **2020**, *246*, 119018. [[CrossRef](#)]
39. Asner, G.P. Cloud cover in Landsat observations of the Brazilian Amazon. *Int. J. Remote Sens.* **2001**, *22*, 3855–3862. [[CrossRef](#)]
40. Mills, S.; Weiss, S.; Liang, C. VIIRS day/night band (DNB) stray light characterization and correction. In Proceedings of the Earth Observing Systems XVIII, International Society for Optics and Photonics, Bellingham, WA, USA, 22–24 August 2013; Volume 8866, p. 88661.
41. Simonetti, D.; Simonetti, E.; Szantoi, Z.; Lupi, A.; Eva, H. First results from the phenology-based synthesis classifier using Landsat 8 imagery. *IEEE Geosci. Remote Sens. Lett.* **2015**, *12*, 1496–1500. [[CrossRef](#)]
42. Zhao, Y.; Gong, P.; Yu, L.; Hu, L.; Li, X.; Li, C.; Zhang, H.; Zheng, Y.; Wang, J.; Zhao, Y.; et al. Towards a common validation sample set for global land-cover mapping. *Int. J. Remote Sens.* **2014**, *35*, 4795–4814. [[CrossRef](#)]
43. Arief, M.C.W.; Itaya, A. A Brief Description of Recovery Process of Coastal Vegetation after Tsunami: A Google Earth Time-Series Remote Sensing Data. *J. Manaj. Hutan Trop.* **2017**, *23*, 81–89. [[CrossRef](#)]
44. Simonetti, E.; Simonetti, D.; Preatoni, D. *Phenology-Based Land Cover Classification Using Landsat 8 Time Series*; European Commission Joint Research Center: Ispra, Italy, 2014.
45. Nguyen, T.T.H.; De Bie, C.; Ali, A.; Smaling, E.; Chu, T.H. Mapping the irrigated rice cropping patterns of the Mekong delta, Vietnam, through hyper-temporal SPOT NDVI image analysis. *Int. J. Remote Sens.* **2012**, *33*, 415–434. [[CrossRef](#)]
46. Huang, H.; Roy, D.P.; Boschetti, L.; Zhang, H.K.; Yan, L.; Kumar, S.S.; Gomez-Dans, J.; Li, J. Separability analysis of Sentinel-2A multi-spectral instrument (MSI) data for burned area discrimination. *Remote Sens.* **2016**, *8*, 873. [[CrossRef](#)]
47. Chen, Y.; Zhang, L.; Li, J.; Shi, Y. Domain driven two-phase feature selection method based on Bhattacharyya distance and kernel distance measurements. In Proceedings of the 2011 IEEE/WIC/ACM International Conferences on Web Intelligence and Intelligent Agent Technology, Lyon, France, 22–27 August 2011; Volume 3, pp. 217–220.
48. Wang, J.; Feng, Z.; Lu, N.; Luo, J. Toward optimal feature and time segment selection by divergence method for EEG signals classification. *Comput. Biol. Med.* **2018**, *97*, 161–170. [[CrossRef](#)]
49. Dabboor, M.; Howell, S.; Shokr, M.; Yackel, J. The Jeffries–Matusita distance for the case of complex Wishart distribution as a separability criterion for fully polarimetric SAR data. *Int. J. Remote Sens.* **2014**, *35*, 6859–6873.
50. Tucker, C.J.; Slayback, D.A.; Pinzon, J.E.; Los, S.O.; Myneni, R.B.; Taylor, M.G. Higher northern latitude normalized difference vegetation index and growing season trends from 1982 to 1999. *Int. J. Biometeorol.* **2001**, *45*, 184–190. [[CrossRef](#)]
51. Roy, P.; Miyatake, S.; Rikimaru, A. Biophysical spectral response modeling approach for forest density stratification. In Proceedings of the 18th Asian Conference on Remote Sensing, Kuala Lumpur, Malaysia, 20–24 October 1997.
52. Kawamura, M.; Jayamanna, S.; Tsujiko, Y. Quantitative evaluation of urbanization in developing countries using satellite data. *Doboku Gakkai Ronbunshu* **1997**, *1997*, 45–54. [[CrossRef](#)]
53. Zha, Y.; Gao, J.; Ni, S. Use of normalized difference built-up index in automatically mapping urban areas from TM imagery. *Int. J. Remote Sens.* **2003**, *24*, 583–594. [[CrossRef](#)]
54. Ettehadi Osgouei, P.; Kaya, S.; Sertel, E.; Alganci, U. Separating built-up areas from bare land in mediterranean cities using sentinel-2a imagery. *Remote Sens.* **2019**, *11*, 345. [[CrossRef](#)]

55. Yang, X.; Zhao, S.; Qin, X.; Zhao, N.; Liang, L. Mapping of urban surface water bodies from Sentinel-2 MSI imagery at 10 m resolution via NDWI-based image sharpening. *Remote Sens.* **2017**, *9*, 596. [[CrossRef](#)]
56. Gascoin, S.; Barrou Dumont, Z.; Deschamps-Berger, C.; Marti, F.; Salgues, G.; López-Moreno, J.I.; Revuelto, J.; Michon, T.; Schattan, P.; Hagolle, O. Estimating fractional snow cover in open terrain from sentinel-2 using the normalized difference snow index. *Remote Sens.* **2020**, *12*, 2904. [[CrossRef](#)]
57. Gitelson, A.A.; Kaufman, Y.J.; Merzlyak, M.N. Use of a green channel in remote sensing of global vegetation from EOS-MODIS. *Remote Sens. Environ.* **1996**, *58*, 289–298. [[CrossRef](#)]
58. Rondeaux, G.; Steven, M.; Baret, F. Optimization of soil-adjusted vegetation indices. *Remote Sens. Environ.* **1996**, *55*, 95–107. [[CrossRef](#)]
59. Huete, A.; Didan, K.; Miura, T.; Rodriguez, E.P.; Gao, X.; Ferreira, L.G. Overview of the radiometric and biophysical performance of the MODIS vegetation indices. *Remote Sens. Environ.* **2002**, *83*, 195–213. [[CrossRef](#)]
60. Lillesand, T.; Kiefer, R.W.; Chipman, J. *Remote Sensing and Image Interpretation*; John Wiley & Sons: Hoboken, NJ, USA, 2015.
61. Li, X.; Zhao, L.; Li, D.; Xu, H. Mapping urban extent using Luojia 1–01 nighttime light imagery. *Sensors* **2018**, *18*, 3665. [[CrossRef](#)]
62. Zimmermann, P.; Tasser, E.; Leitinger, G.; Tappeiner, U. Effects of land-use and land-cover pattern on landscape-scale biodiversity in the European Alps. *Agric. Ecosyst. Environ.* **2010**, *139*, 13–22. [[CrossRef](#)]
63. Murad, C.A.; Pearse, J. Landsat study of deforestation in the Amazon region of Colombia: Departments of Caquetá and Putumayo. *Remote Sens. Appl. Soc. Environ.* **2018**, *11*, 161–171. [[CrossRef](#)]
64. Farjad, B.; Gupta, A.; Razavi, S.; Faramarzi, M.; Marceau, D.J. An integrated modelling system to predict hydrological processes under climate and land-use/cover change scenarios. *Water* **2017**, *9*, 767. [[CrossRef](#)]
65. Samal, D.R.; Gedam, S.S. Monitoring land use changes associated with urbanization: An object based image analysis approach. *Eur. J. Remote Sens.* **2015**, *48*, 85–99. [[CrossRef](#)]
66. Wang, R.; Kalin, L.; Kuang, W.; Tian, H. Individual and combined effects of land use/cover and climate change on Wolf Bay watershed streamflow in southern Alabama. *Hydrol. Process.* **2014**, *28*, 5530–5546. [[CrossRef](#)]
67. Kang, J.; Yang, X.; Wang, Z.; Cheng, H.; Wang, J.; Tang, H.; Li, Y.; Bian, Z.; Bai, Z. Comparison of Three Ten Meter Land Cover Products in a Drought Region: A Case Study in Northwestern China. *Land* **2022**, *11*, 427. [[CrossRef](#)]
68. Venter, Z.S.; Barton, D.N.; Chakraborty, T.; Simensen, T.; Singh, G. Global 10 m Land Use Land Cover Datasets: A Comparison of Dynamic World, World Cover and Esri Land Cover. *Remote Sens.* **2022**, *14*, 4101. [[CrossRef](#)]
69. Alava Portugal, C.; Hechavarría Hernández, J.R.; Fois Lugo, M. Systemic approach to the territorial planning of the urban Parish La Aurora, Daule, Ecuador. In Proceedings of the International Conference on Intelligent Human Systems Integration, Modena, Italy, 19–21 February 2020; Springer: Berlin/Heidelberg, Germany, 2020; pp. 1201–1205.
70. Zambrano Murillo, C.; Hechavarría Hernández, J.R.; Leyva Vázquez, M. Environmental Certification Proposal for Sustainable Buildings in the Satellite Parish “La Aurora”, Guayas, Ecuador. In Proceedings of the International Conference on Applied Human Factors and Ergonomics, San Diego, CA, USA, 16–20 July 2020; Springer: Berlin/Heidelberg, Germany, 2020; pp. 63–70.
71. López, S. Deforestation, forest degradation, and land use dynamics in the Northeastern Ecuadorian Amazon. *Appl. Geogr.* **2022**, *145*, 102749. [[CrossRef](#)]
72. Santos, F.; Meneses, P.; Hostert, P. Monitoring long-term forest dynamics with scarce data: A multi-date classification implementation in the Ecuadorian Amazon. *Eur. J. Remote Sens.* **2019**, *52*, 62–78. [[CrossRef](#)]
73. Moulatlet, G.M.; Ambriz, E.; Guevara, J.; Lopez, K.G.; Rodes-Blanco, M.; Guerra-Arevalo, N.; Ortega-Andrade, H.M.; Meneses, P. Multi-taxa ecological responses to habitat loss and fragmentation in western Amazonia as revealed by RAPELD biodiversity surveys. *Acta Amaz.* **2021**, *51*, 234–243. [[CrossRef](#)]

Disclaimer/Publisher’s Note: The statements, opinions and data contained in all publications are solely those of the individual author(s) and contributor(s) and not of MDPI and/or the editor(s). MDPI and/or the editor(s) disclaim responsibility for any injury to people or property resulting from any ideas, methods, instructions or products referred to in the content.